# MODELING, SYSTEM OPTIMIZATION AND ARTIFACT REDUCTION IN MAGNETIC INDUCTION TOMOGRAPHY FOR MEDICAL APPLICATIONS

A DISSERTATION SUBMITTED TO
THE FACULTY OF ELECTRICAL ENGINEERING
OF
GRAZ UNIVERSITY OF TECHNOLOGY

BY

DOĞA GÜRSOY

IN PARTIAL FULFILLMENT OF THE REQUIREMENTS
FOR
THE DEGREE OF DOCTOR OF PHILOSOPHY
IN
ELECTRICAL ENGINEERING

FEBRUARY 2010

# ABSTRACT

MODELING, SYSTEM OPTIMIZATION AND ARTIFACT REDUCTION IN MAGNETIC INDUCTION TOMOGRAPHY FOR MEDICAL APPLICATIONS

Gürsoy, Doğa
PhD, Institute of Medical Engineering
Supervisor: Ao.univ.-prof. Dipl.-ing. Dr.techn. Hermann Scharfetter

February 2010

Magnetic induction tomography (MIT) is an emerging imaging modality and aims to reconstruct the electrical tissue properties in the region of interest. The noncontact and noninvasive measurement characteristics together with the fast scanning ability make the proposed modality attractive. It promises to facilitate diagnosis of several physiological disorders such as oedema or internal hemorrhage and has the potential to be used for the continuous monitoring of pathological fluid changes. This study focuses on improving the image quality and the investigation of several fundamental issues that must be tackled in order to have the modality as a diagnostic tool alongside clinical standard imaging modalities. To this end, several alternative coil configurations have suggested and the resulting imaging quality was compared with that of currently existing systems. Furthermore an optimization approach for the optimization of the coil design was developed. For this, the image performance measures are reviewed and a measure which favors the coil designs with the

most independent information content is used to reach optimal designs. Besides the coil optimization, another important issue affecting image quality is the correction of patient positioning errors and movement artifacts in the numeric models. These errors were analyzed in simulation studies ands several solution strategies were proposed to compensate the artifacts. Lastly it was investigated to what extent the anisotropic electrical characteristics of the tissues must be considered in the forward and inverse models so as to keep reconstruction errors small. An anisotropic inverse solver was developed and the results were compared with those of a conventional isotropic solver. In particular conductivity tensor images were reconstructed to explore the effect of surface-near muscle tissue.

Keywords: Magnetic induction tomography, optimal design, coil optimization, image reconstruction, movement artifacts, tissue anisotropy

To my parents...

# ACKNOWLEDGMENTS

I have had the rare privilege and opportunity to work with many talented individuals during my study. Without their support and contributions, this dissertation would not have been possible. First, I sincerely thank my supervisor Hermann Scharfetter for his excellent guidance, motivation and criticisms throughout the research. He has always been an inspirational mentor and a role model to me. I also express my gratitude to Manuel Freiberger for the insightful discussions on the topic and other colleagues Florian Knoll, Bernhard Neumayer and Michael Hofer for their moral supports and friendship. This is also a great opportunity to express my respect to Olaf Steinbach, Sarah Engleder, Herbert Egger and Sabine Zaglmayer for their collaboration and assistance concerning mathematical issues. My special thanks are to Gözde Göksu for her love, patience and friendship that have kept me focused and motivated over those years and to my parents for their guidance, support and encouragement to pursue my graduate studies from the beginning. Finally, I appreciate the financial support granted by the Austrian Science Fund under the SFB project F32-N18 and Graz University of Technology for supporting several travel and meeting expenses that I have attended throughout the study.

# TABLE OF CONTENTS

ABSTRACT . . . . . ii

ACKNOWLEDGMENTS . . . . . v

TABLE OF CONTENTS . . . . . vi

LIST OF TABLES . . . . . ix

LIST OF FIGURES . . . . . x

1. INTRODUCTION . . . . . 1

1.1 Overview . . . . . 1

1.2 History . . . . . 1

1.3 Motivations and Objectives . . . . . 3

1.4 Outline . . . . . 5

2. FORWARD PROBLEM . . . . . 6

2.1 Introduction . . . . . 6

2.2 Formulation . . . . . 6

2.2.1 Maxwell's Equations . . . . . 6

2.2.2 Potential Field Approach . . . . . 7

2.2.3 Gauge Fixing . . . . . 7

2.2.4 Quasi-Stationary Approximations . . . . . 8

2.2.5 Measurements . . . . . 8

2.2.5.1 Reciprocal Approach . . . . . 8

2.2.5.2 Direct Approach . . . . . 9

2.3 Solution Strategies . . . . . 9

2.3.1 Magnetic Vector Potential . . . . . 9

2.3.2 Electric Scalar Potential . . . . . 10

2.3.2.1 Finite Element Discretization . . . 10

2.3.2.2 Linear Solvers . . . . . 11

3. INVERSE PROBLEM . . . . . 12
3.1 Introduction . . . . . 12
3.2 Problem Definition . . . . . 12
3.3 Solution Strategies . . . . . 13
3.3.1 Regularized Gauss-Newton Method . . . . . 13
3.3.1.1 Single Iteration . . . . . 14
3.3.1.2 Subsequent Iterations . . . . . 14
3.3.2 Truncated Singular Value Decomposition . . . 15
4. SYSTEM OPTIMIZATION . . . . . 16
4.1 Introduction . . . . . 16
4.2 Effect of Coil Orientations on Imaging . . . . . 16
4.2.1 Evaluation Criteria . . . . . 17
4.2.1.1 Image Resolution and Uncertainty . 17
4.2.1.2 Generalized Quality Measures . . . 18
4.2.2 Simulation Setup . . . . . 19
4.2.3 Results . . . . . 22
4.2.4 Discussions . . . . . 27
4.3 Optimal Coil Positioning . . . . . 29
4.3.1 Optimization Algorithm . . . . . 29
4.3.2 Simulation Setup . . . . . 31
4.3.3 Results . . . . . 33
4.3.4 Discussions . . . . . 38
4.4 Conclusion . . . . . 41
5. ARTIFACT REDUCTION . . . . . 43
5.1 Introduction . . . . . 43
5.2 Movement Effects . . . . . 43
5.2.1 Simulation Setup . . . . . 44
5.2.2 Evaluation Criteria . . . . . 47
5.2.3 Filtering Strategy . . . . . 47
5.2.4 Results . . . . . 47
5.2.5 Discussions . . . . . 50
5.3 Modeling Anisotropy . . . . . 53
5.3.1 Anisotropy Tensor Imaging . . . . . 53

5.3.2 Simulation Setup . . . . . 54
5.3.3 Results . . . . . 57
5.3.4 Discussions . . . . . 60
5.4 Conclusion . . . . . 61
6. FUTURE DIRECTIONS . . . . . 63
APPENDICES . . . . . 74
A. MAGNETIC VECTOR POTENTIAL . . . . . 74
B. OPTIMIZATION MEASURE . . . . . 75
VITA . . . . . 76
PUBLICATIONS . . . . . 77

# LIST OF TABLES

TABLES

4.1 Optimum truncation levels for the designs corresponding to different SNR levels. (-) means that no truncation is necessary. 22
4.2 Total resolution ($tr(\mathbf{S}^{\dagger}\mathbf{S})$) of (A) the central slice and (B) the slice at z = 5 $cm$ for the corresponding designs. . . . . 40

5.1 The conductivity values in S $m^{-1}$ of the simulation model shown in figure 5.9. . . . . 56

# LIST OF FIGURES

FIGURES


4.1 The cylindrical phantom and the positioning of the transmitter coils. The left and the right diagrams correspond to the side view and the top view. All units are given in millimetres. . . . 20

4.2 Demonstration of the receiver coil designs: (a) $D1$, (b) $D2$, (c) $D3$, (d) $D4$, (e) $D5$ and (f) $D6$. . . . . 20

4.3 The logarithmic ratio between the first and the $k^{th}$ singular value as compared to the SNR. . . . . 21

4.4 The curves of the normalized resolution and variance measures at 20 dB SNR level along the z-axis corresponding to the designs. The slices at 5 and 7 cm on the z-axis were marked as dotted vertical lines to highlight the locations of the perturbations. On the y-axes, 0 and 1 indicates the minimum and the maximum, respectively. . . . . 23

4.5 The curves of the normalized resolution and variance measures at 20 dB SNR level along the radial-axis considering different slices. The radial position at 6 cm was marked as a dotted vertical line on the radial-axis to highlight the locations of the perturbations. On the y-axes, 0 and 1 indicates the minimum and the maximum, respectively. . . . . 23

4.6 The normalized quality curves along the z-axis ($\alpha = 1$) corresponding to the designs. The slices at 5 and 7 cm on the z-axis were marked as dotted vertical lines to highlight the locations of the perturbations. On the y-axis, 0 and 1 indicates the minimum and the maximum, respectively. . . . . 24

4.7 The effect of SNR on the design qualities of the designs ($\alpha = 1$). The slices at 5 and 7 cm on the z-axis were marked as dotted vertical lines to highlight the locations of the perturbation . . . . . 25

4.8 The images reconstructed from the corresponding designs using noise-free data. From left column to the right column: (a) D1, (b) D2, (c) D3, (d) D4, (e) D5 and (f) D6, respectively. . . 26

4.9 The images reconstructed from different designs using noisy data of 20 dB SNR. The truncation was applied according to table 2. From left column to the right column: (a) D1, (b) D2, (c) D3, (d) D4, (e) D5 and (f) D6, respectively. . . . . 27

4.10 Transmitter arrangements around the cylindrical phantom (0.1 S $m^{-1}$) which has 3 local spherical inhomogeneities (0.2 S $m^{-1}$). (a) 8 flat transmitter coil geometries [T1] and (b) 16 crosswise transmitter coil geometries [T2] were used for excitation. Upper diagrams are the top views and lower ones are the side views of the simulation arrangements. All distance units are in cm. . . . . 32

4.11 The possible receiver locations selected for the initialization of the design optimization. (a) side view and (b) top view. . . . . 33

4.12 Optimum receiver designs for T1. The dashed area at each phantom represents the region of which the information content is maximized. (a) the design [R1] without focusing. (b) The design [R2] obtained by focusing to the the slice at z = 5 cm. (c) The design [R3] obtained by focusing to the central slice. . 34

4.13 Reconstructions with the optimum receiver designs by using T1 as excitation. (a) the reconstruction obtained using R1 without focusing. (b) The reconstruction obtained using R2 which focuses to the the slice at z = 5 cm. (c) The reconstruction obtained using R3 which focuses to the central slice. . . . 35

4.14 Optimum receiver designs for T2. The dashed area at each phantom represents the region of which the information content is maximized. (a) The design [Ra] without focusing. (b) The design [Rb] obtained by focusing to the the slice at z = 5 cm. (c) The design [Rc] obtained by focusing to the central slice. . . . . 36

4.15 Reconstructions with the optimum receiver designs by using T2 as excitation. (a) the reconstruction obtained using Ra without focusing. (b) The reconstruction obtained using Rb which focuses to the the slice at z = 50 cm. (c) The reconstruction obtained using Rc which focuses to the central slice. 37

4.16 The corresponding eigenvalues of the Hessian matrices obtained from R1, R2 and R3 as receiver designs and T1 as the excitation scheme. . . . . 38

4.17 The eigenvalues of the Hessian matrices obtained from Ra, Rb and Rc as receiver designs and T2 as the excitation scheme. Only the coloumns of the sensitivity matrix which corresponds to the central slice were used for the calculation of the Hessian. 39

4.18 The corresponding eigenvalues of the Hessian matrices obtained from R1 and Ra as receiver designs and T1 and T2 as the excitation schemes. For convenience, only the largest 128 of 512 eigenvalues are plotted for T2-Rc design. . . . . 39

5.1 Simulation arrangement for solving the inverse problem and generating simulated voltage data: (a) transmitter setup, (b) receiver setup. All measures are in cm. . . . . 45
5.2 Modelling of body movements. Shifts from the original position were chosen as 2 and 4 mm which corresponds to 10% and 20% change in the distance between the surface of the phantom and the receivers. All movements are assumed to be on transversal plane . . . . . 46
5.3 Noise free reconstructions. . . . . 48
5.4 Reconstructions with 20 dB noise. . . . . 49
5.5 PMCC between the undistorted image and the images which were obtained with different types of movements during data acquisition. . . . . 50
5.6 Illustration of the filtering strategy used to remove movement artifacts. . . . . 51
5.7 The frequency differential images obtained by assigning the (left) same and (right) different conductivity values to the background for seperate states of data simulation. . . . . 52
5.8 Simulation setup. . . . . 55
5.9 The cylindrical phantoms with different anisotropic electrical properties used in simulations. . . . . 56
5.10 (a) Conductivity reconstruction of the central slice using an isotropic solver. Reconstruction of different conductivity tensor components: (b) $\Delta\sigma_{xx}$ reconstruction, (c) $\Delta\sigma_{yy}$ reconstruction. . . . . 57
5.11 Various conductivity distribution reconstructions of the central slice obtained by applying different initializations and sensitivity maps. . . . . 59

# CHAPTER 1

# INTRODUCTION

## 1.1 Overview

Magnetic induction tomography (MIT) is an emerging modality for reconstructing the electrical tissue properties in a region of interest of the human body and has attracted considerable attention since the 1990s. It promises to facilitate diagnosis of several physiological disorders such as oedema or internal hemorrhage and has the potential to be used for continuous monitoring of physiological fluids. Several features of the device such as high temporal resolution, portability, noncontact and noninvasive measurement characteristics make the proposed modality attractive. To date, several prototype MIT systems have been built and the viability of the method has been confirmed by feasibility studies. However, despite the considerable progress that has been made in the last decade, the imaging performance of the prototypes is still not sufficient for clinical trials. This work addresses some of the fundamental issues that must be tackled in order to have the modality as a diagnostic tool alongside the other standard imaging modalities.

## 1.2 History

Imaging the passive electrical properties of the human body has gained an enormous interest among scientists to date [Holder, 1993, 1995]. However, using electrode based measurements that use direct contacts with the body surface has some formidable drawbacks like the poor skin-electrode contact

[Boone and Holder, 1996a,b] and the reduced penetration of injected currents into certain regions due to insulating layers, such as bone [Gençer and İder, 1994]. In the early 1990s, instead of using electrodes, a coil based method based on Faraday's law of induction was proposed as an alternative method to obtain conductivity tomographies [Al-Zeibak and Saunders, 1993]. In the proposed method, an eddy current density is induced within the human body via transmitter coils and the magnetic field is measured using an array of sensor coils in a non-contact manner to reconstruct tomographies. This method is today widely accepted as magnetic induction tomography [Griffiths et al., 1999, Korjenevsky and Cherepenin, 1997, 1999, Scharfetter et al., 2001]. Additionally, the non-contact nature of the method brings easiness to data-acquisition by enabling to collect further measurements by simply shifting the coil arrays [Griffiths, 2001].

The first imaging attempts were carried out by a linear-backprojection method to obtain tomographies from a set of measurement data [Al-Zeibak and Saunders, 1993, Korjenevsky et al., 2000]. This image reconstruction approach has been found to be flawed today [Scharfetter et al., 2002] and substituted by more advanced methods that approximate the sensitivity distribution of the measurements correctly [Hollaus et al., 2004b, Merwa et al., 2005, Pham and Peyton, 2008b, Rosell et al., 2001, Soleimani, 2006]. In these studies, the sensitivity maps were computed according to the reciprocity theorem [Mortarelli, 1980]. To this end, the solution of Maxwell's equations [Malmivuo and Plonsey, 1995] are required. It was reported that the quasi-stationary regime is computationally more convenient for low frequency applications [Gençer et al., 1994, Gürsoy, 2007]. However, in order to achieve accuracy at higher frequencies, the complete wave equations in a dielectric media must be solved [Hollaus et al., 2004a, Soleimani et al., 2006]. The finite element method is usually the method of choice [Gençer and Tek, 1999a,b, Ktistis et al., 2008, Merwa et al., 2003, Soleimani et al., 2006], however, finite differences [Morris et al., 2001, Gürsoy, 2007] and boundary element methods [Pham and Peyton, 2008a] have also been employed.

In MIT, the change in the magnetic field due to the conductivity perturbation is much weaker than the primary magnetic field which leads to a narrow dynamic range in the receiver channels [Griffiths, 2001]. Up to now, much effort has been expended with the aim of reaching an efficient coil configuration to extend the dynamic range of the measured signal. For this purpose, flux cancellation techniques like back off coils [Griffiths et al., 1999], specially oriented sensors [Igney et al., 2005, Scharfetter et al., 2004, Watson et al., 2004, 2005], and gradiometers realized on printed circuit boards (PCB) [Merwa and Scharfetter, 2008, Scharfetter et al., 2005] or as coils [Karbeyaz and Gençer, 2003, Riedel et al., 2004] have been extensively analyzed. Corresponding imaging performance and detectability features have been analyzed based on the point spread functions [Merwa and Scharfetter, 2007, Scharfetter et al., 2006].

The frequency dependence of the electrical properties of tissues has been known for years [McAdams and Jossinet, 1995, Osypka and Gersing, 1995]. The methodology, when applied at multiple frequencies [Brunner et al., 2006, Scharfetter et al., 2003, Rosell et al., 2006], is specifically attractive for monitoring of several disorders in the human body such as oedema [Kao et al., 1991], hemorrhages or epileptic seizures which are correlated with local fluid shifts. To date, the detectability of fluid changes in the brain has been investigated by numerous researchers for simple geometries [Hart et al., 1988, Netz et al., 1993, Xu et al., 2009] and for realistic head geometries based on MRI or CT scans [Merwa et al., 2004, Gürsoy, 2007, Zolgharni et al., 2009a,b]. Although, the ongoing research supplies ample findings to the detectability of fluid shifts, it also attracts attention to the advancements necessary to achieve a successful in vivo imaging modality.

## 1.3 Motivations and Objectives

1. *Developing a fast numerical solver:* Image reconstruction in MIT requires consecutive solution of the forward problem for all sets of excitation-measurement pairs which is computationally demanding concerning complex valued, large-scale problems. For low frequency applications, it

was reported that the quasi-stationary approximation holds and this approximation reduces the need for memory and computational resources substantially. Furthermore, some biological tissues show up anisotropic electrical properties which has not been modeled previously and it still remains an open question whether the conventional modeling approaches used so far are appropriate or not for clinical applications. Therefore, a numerical finite element model is aimed to be developed for the computation of quasi-static electromagnetic fields in an arbitrary shaped, inhomogeneous and anisotropic media nearby a transmitting coil. Additionally, several preconditioning and solution techniques shall be experimented to investigate the convergence characteristics to accelerate the solutions.

2. *System optimization:* The experimental MIT systems that have so far been built are designed with 16 measurement sensors that encircle the region of interest. The imaging quality of possible other configurations have not been explored in detail, though, the location and orientation of the sensors considerably affect the measurements and also the performance of the image reconstruction. Therefore, in this study several alternative configurations shall be tested in terms of imaging quality such as spatial resolution and variance. Instead of using heuristic experiments, the problem shall also be defined as an optimization problem to end up with optimal designs in a feasible amount of time.

3. *Investigation of artifacts due to patient's movement:* In clinical usage, the patient can move during the data acquisition and how much this affects the reconstructed images is an open question. Especially, for chest applications this movement is inevitable unless a breath-hold protocol during measurements is feasible. Therefore, the effect of the patient's movement during data acquisition to the reconstructed images shall be determined and some possible solutions shall be proposed to compensate this effect.

## 1.4 Outline

This Chapter provides an overview and history of the field and presents the rationale for the study. Chapter 2 mathematically describes the forward relationship between the electrical tissue properties and the measurements of the modality. The electromagnetic formulation for an inhomogeneous, linear and arbitrary shaped media is derived from Maxwell's equations and corresponding solution approaches are summarized. Chapter 3 reviews the MIT inverse problem and addresses the corresponding solution strategies. Chapter 4 focuses on system optimization and discusses the effect of coil positioning on the imaging performance. It also provides a method to reach optimal designs in a feasible amount of time. Chapter 5 discusses the modeling improvements that must be achieved for successful in vivo imaging. The importance of model correction to get rid of the artifacts due to the patient's movements inside the tomograph is underlined and some possible compensation techniques are proposed. Besides, the effect of anisotropy on images and the feasibility of tensor imaging is investigated. The last Chapter summarizes the study and sets a course for those who wish to work on this field and expand the study.

# CHAPTER 2

# FORWARD PROBLEM

## 2.1 Introduction

The forward problem of MIT is defined as, given the electrical properties of the medium, finding the induced voltages in the receiver coil due to the eddy-currents evoked by the time-harmonic excitation. The corresponding formulation is based on the Maxwell's electromagnetic field equations which has been reported in various studies. The well-known approach for the solution is the potential field formulation that uses auxillary potentials, i.e. the magnetic potential $\mathbf{A}$ and the electric potential $\phi$, for the representation of the fields [Bíro, 1999]. This chapter will review the formulation of the forward problem and possible solution strategies for the corresponding equations.

## 2.2 Formulation

### 2.2.1 Maxwell's Equations

Let the solution domain consist of a conducting medium $\Omega_c$ and a surrounding nonconducting region $\Omega_n$ such that $\Omega = \Omega_c \cup \Omega_n$. The forward problem is defined as, given the electrical properties of the medium $\Omega_c$, finding the induced voltages in the receiver coil due to the eddy-currents evoked by an impressed current density $\mathbf{J}_s$ in a source region $\Omega_s$. Mathematically speaking, referring to the constitutive relations for a linear and an isotropic material behaviour as $\mathbf{B} = \mu\mathbf{H}$, $\mathbf{D} = \epsilon\mathbf{E}$ and $\mathbf{J} = \sigma\mathbf{E}$, the following Maxwell's equations describe

the time-harmonic electromagnetic fields in a dielectric medium:

$$\nabla \times \mathbf{E} = -jw\mathbf{B} \tag{2.1}$$

$$\nabla \times \mathbf{H} = \kappa\mathbf{E} + \mathbf{J}_s \tag{2.2}$$

$$\nabla \cdot \mathbf{D} = \rho \tag{2.3}$$

$$\nabla \cdot \mathbf{B} = 0, \tag{2.4}$$

where **E**, **H**, **B** and **D** are the electric field, magnetic field, magnetic flux density, electric displacement, respectively. The material properties $\mu$ and $\kappa = \sigma + jw\epsilon$ represent the electrical permeability and admittivity of the conducting medium. The time-harmonic dependence is represented with angular frequency $\omega$.

### 2.2.2 Potential Field Approach

Using (2.1) and (2.4), **E** and **B** can be described uniquely by use of the auxillary potentials, i.e., the magnetic potential **A** and the electric potential $\phi$, as follows,

$$\mathbf{B} = \nabla \times \mathbf{A} \tag{2.5}$$

$$\mathbf{E} = -\nabla\phi - jw\mathbf{A}. \tag{2.6}$$

When the above equations are plugged into (2.2) and (2.3), the formulation of the potential field equations becomes complete with the below equations,

$$\nabla \times (\mu^{-1}\nabla \times \mathbf{A}) - \kappa(-\nabla\phi - jw\mathbf{A}) = \mathbf{J}_s \tag{2.7}$$

$$\nabla \cdot \kappa(-\nabla\phi - jw\mathbf{A}) = 0. \tag{2.8}$$

### 2.2.3 Gauge Fixing

Although, the auxilary potentials **A** and $\phi$ uniqely describe the electromagnetic fields **E** and **B**, the reverse is not true. For instance, by using a differentiable scalar function $\psi$, infinitely many **A** and $\phi$ can be found in the form of $\mathbf{A}+\nabla\psi$ and $\phi - jw\psi$ which satisfy (2.7) and (2.8). Coloumb's gauge is commonly the

method of choice considering inhomogenous domains and when imposed on $\mathbf{A}$, the following equations come out,

$$\nabla^2\mathbf{A} + jw\mu\kappa(-\nabla\phi - jw\mathbf{A}) = -\mu\mathbf{J}_s \quad (2.9)$$

$$-\nabla\cdot\kappa\nabla\phi - jw\mathbf{A}\cdot\nabla\kappa = 0. \quad (2.10)$$

### 2.2.4 Quasi-Stationary Approximations

For low frequency biomedical applications, the impressed current density $\mathbf{J}_s$ in $\Omega_s$ is much larger than induced eddy-currents in $\Omega_c$. Therefore, the contribution of the term $jw\mu\kappa(-\nabla\phi - jw\mathbf{A})$ to the excitation field is commonly neglected [Gençer et al., 1994]. This results in the following quasi-static representaion of (2.9),

$$\nabla^2\mathbf{A} = -\mu\mathbf{J}_s. \quad (2.11)$$

Therefore, $\mathbf{A}$ can be calculated from (2.11) and directly used as a source term in (2.10) for the computation of the scalar potential $\phi$. By applying the boundary condition that the normal component of the current density must be zero on $\Omega_c \cap \Omega_n$, the relationship between $\phi$ and $\mathbf{A}$ is expressed as,

$$\nabla\cdot\kappa\nabla\phi = -jw\mathbf{A}\cdot\nabla\kappa \quad \in \Omega_c \quad (2.12)$$

$$\kappa\nabla\phi\cdot\mathbf{n} = -jw\kappa\mathbf{A}\cdot\mathbf{n} \quad \in \Omega_c \cap \Omega_n, \quad (2.13)$$

where $\mathbf{n}$ is the normal vector pointing outward from the boundary of the conducting medium.

### 2.2.5 Measurements

#### 2.2.5.1 Reciprocal Approach

According to the Rayleigh-Carson reciprocity theorem, time-harmonic current densities and corresponding electromagnetic fields can be interchanged under certain circumstances. Referring $\mathbf{E}_R$ as the virtual electric field due to a unity reciprocal current density in the receiver coil, the induced voltage in that coil can be written as,

$$v = \int_{\Omega_c} \kappa\mathbf{E}\cdot\mathbf{E}_R d^3r, \quad (2.14)$$

where the integration is taken over the conducting domain $\Omega_c$. $\kappa\mathbf{E}$ denotes the induced currents due to the transmitter excitation.

In a similar manner, the reciprocity theorem can as well be defined on the domain $\Omega_r$ where the receiver coil is present. Considering an infinitely thin and circular coil, the induced voltages in that coil can be obtained as follows,

$$v = \int_{\Omega_r} \mathbf{E} \cdot \mathbf{J}_R dr, \tag{2.15}$$

where $dr$ denotes the infinitely small line elements. If the reciprocal current $\mathbf{J}_R$ is unity, then from Faraday's law of induction, (2.15) is equivalent to (2.14).

#### 2.2.5.2 Direct Approach

Once the electromagnetic fields in $\Omega_c$ are solved, the induced voltage in a circular receiver coil can be obtained by,

$$v = -jw \int_{S_r} \mathbf{B} \cdot \mathbf{n} d^2 r, \tag{2.16}$$

where the integration is taken over the closed circular surface of the coil $S_r$ and $\mathbf{n}$ is the normal vector orthogonal to that plane. $\mathbf{B}$ represents the magnetic field due to the eddy-current density and is computed from the Biot-Savart law,

$$\mathbf{B} = \frac{\mu}{4\pi} \int_{\Omega_c} \kappa\mathbf{E} \times \frac{\mathbf{r}}{r^3} d^3 r, \tag{2.17}$$

where $\mathbf{r}$ represents the vector from source point in $\Omega_c$ to the field point in $S_r$ and $r$ is the corresponding distance. This method requires a numerical integration over the coil area as described by (2.16) and becomes computationally more efficient over the reciprocal method when the receiver coils are small.

## 2.3 Solution Strategies

### 2.3.1 Magnetic Vector Potential

The solution of (2.11) for the magnetic vector potential $\mathbf{A}$ at location $r$ in $\Omega_c$ can be obtained from,

$$\mathbf{A}(r) = \frac{\mu_0}{4\pi} \int \frac{\mathbf{J}_s(r')}{|r - r'|} d^3 r' \quad r \in \Omega_c, \tag{2.18}$$

where $r'$ represents the source points in $\Omega_s$. This equation can simply be solved either by numerical quadrature or by incorporating analytical methods and shall be explained in the appendix.

### 2.3.2 Electric Scalar Potential

Solution of (2.12) and (2.13) for the electric scalar potential in $\Omega_c$ is not trivial for arbitrary shaped conducting domains and analytical methods are not available. Thus, it is essential to apply numerical methods for the computation of $\phi$.

#### 2.3.2.1 Finite Element Discretization

By using Galerkin's weighted residual method to discretisize the partial differential equation,

$$\int_{\Omega_c} N_i \nabla \cdot \kappa \nabla \phi d^3 r = -\int_{\Omega_c} N_i jw\mathbf{A} \cdot \nabla \kappa d^3 r, \tag{2.19}$$

where the subscript $i$ denotes the $i^{th}$ shape function. By using the appropriate vector identities and applying the Divergence theorem to the resultant expressions, the equations become,

$$\int_{\Omega_c} \kappa \nabla N_i \cdot \nabla \phi d^3 r = -\int_{\Omega_c} \kappa \nabla \cdot (N_i jw\mathbf{A})\, d^3 r, \tag{2.20}$$

where the surface integral terms drops due to the condition $\kappa \nabla \phi_n = -jw\kappa \mathbf{A}_n$. By applying again the Divergence theorem to the right hand side of (2.20), we get,

$$\int_{\Omega_c} \kappa \nabla N_i \cdot \nabla \phi d^3 r = -\int_{\partial\Omega_c} N_i jw\kappa \mathbf{A} \cdot d^2 \mathbf{r}, \tag{2.21}$$

where,

$$\nabla \phi = \sum_{j=1}^{k} \nabla N_j \phi_j, \tag{2.22}$$

where $k$ represents the number of equations for each element. In this study, tetrahedral elements of first order were used for spatial discretization. Once the element matrices have been formed, they are used to fill the linear set of equations to form a matrix equation as given,

$$\mathbf{K}\phi = \mathbf{b}. \tag{2.23}$$

#### 2.3.2.2 Linear Solvers

Considering complex valued, large-scale problems as defined in (2.23), it is more convenient to apply iterative methods for solving the electric scalar potential $\phi$. Knowing that the coefficient matrix $\mathbf{K}$ is sparse, symmetric and indefinite, quasi-minimual residual method was applied for the solution [Bollhöfer and Saad, 2006].

The solutions can further be accelerated by using an appropriate preconditioner to (2.23). Mathematically speaking, applying a preconditioner can be considered as transforming the linear system into an equivalent system of which the convergence is achieved faster. In that manner, a preconditioner to the linear system in (2.23) is represented by a matrix $\mathbf{M}$ that satisfies the following,

$$\mathbf{M}^{-1}\mathbf{K}\phi = \mathbf{M}^{-1}\mathbf{b}. \tag{2.24}$$

The desired preconditioner is the one that makes the condition number of $\mathbf{M}^{-1}\mathbf{K}$ as close to unity as possible and must be invertible efficiently.

Recently, an inverse-based multi-level ILU preconditioning scheme was proposed for complex valued sparse matrices of general structure [Bollhöfer and Saad, 2006] and was applied for preconditioning of the linear system of equations as given in (2.23).

# CHAPTER 3

# INVERSE PROBLEM

## 3.1 Introduction

The inverse problem of MIT is defined as reconstructing the conductivity distribution of the human body from a set of measurement data. Let the relation between the measurements and the conductivity be expressed as, $v = \psi(\sigma)$, where $\psi$ is a nonlinear function acting on a given conductivity, $\sigma$. The corresponding inverse problem, $\sigma = \psi^{-1}(v)$, is severely ill-posed, namely, small changes in measurements cause large changes in the solution. The most commonly used approach to address this problem is to impose a *priori* information and adopt regularization methods to overcome ill-posedness. The solutions are obtained assuming linearity and solving for the small perturbations around a reference conductivity distribution. Thus, for a feasible reconstruction, the awareness of the expected solution, in other words, a good initialization, is essential to cope with the difficulties related to nonlinearity. This chapter presents the formulation and common solution strategies to that problem.

## 3.2 Problem Definition

The sensitivity of the data to the conductivity perturbations can be approximated from (2.16) as,

$$\frac{\partial v_{ij}}{\partial \sigma} = \Delta\sigma^{-1} \int_{\Omega_c} \Delta\sigma \mathbf{E}_i \cdot \mathbf{E}_j d^3r, \tag{3.1}$$

or from (2.14) as follows,

$$\frac{\partial v_{ij}}{\partial \sigma} = -\frac{jw\mu_0}{4\pi\Delta\sigma}\int_{\Omega_j}\left(\int_{\Omega_c}\Delta\sigma\mathbf{E}_i \times \frac{\mathbf{r}}{r^3}d^3r\right)\cdot d^2\mathbf{r}, \tag{3.2}$$

where $\Delta\sigma$ denotes the conductivity deviations from a reference distribution. Therefore, assuming admissible conductivity fluctuations, by using (3.1) or (3.2), the following system of linear equations can be formed,

$$\mathbf{S}\Delta\sigma = \Delta v, \tag{3.3}$$

where $\mathbf{S}$ is referred to as the sensitivity matrix. Each row corresponds to one transmit-receive coil pair and each column to one voxel. Within the range of linearity, a fairly convenient solution for $\Delta\sigma$ can be obtained from,

$$\Delta\sigma = \mathbf{S}^{\dagger}\Delta v, \tag{3.4}$$

by defining $\mathbf{S}^{\dagger}$ as the generalized inverse of $\mathbf{S}$.

## 3.3 Solution Strategies

### 3.3.1 Regularized Gauss-Newton Method

Tikhonov regularization is widely used to increase the conditioning of the system of equations [Merwa et al., 2005, 2006, Scharfetter et al., 2006, Ziolkowski et al., 2009]. This type of regularization commonly causes smooth solutions. The regularized least-squares solution for $\Delta\sigma$ can be obtained by minimizing the $L_2$-norm of the residuals between the estimated and measured data as defined by means of a minimization problem,

$$\Delta\sigma = \operatorname{argmin}\left(\frac{1}{2}\left\|\mathbf{S}\Delta\sigma - \Delta v\right\|^2 + \frac{\lambda}{2}\left\|\mathbf{R}\Delta\sigma\right\|^2\right), \tag{3.5}$$

where $\mathbf{R}$ is the regularization matrix and $\lambda$ is the regularization parameter that specifies the amount of applied regularization. It is possible to choose $\mathbf{R}$ differently. This study uses only the identity matrix as a regularization matrix, however, several other regularization matrices such as neighboring matrix and matrices that minimize spatial variance have been reported previously [Merwa et al., 2004, Scharfetter et al., 2006].

#### 3.3.1.1 Single Iteration

A single iteration of the Gauss-Newton algorithm gives a fairly convenient solution for $\Delta\sigma$ and can be used for the solution of the minimization problem given in (3.5). The corresponding solution can be obtained from,

$$\Delta\sigma = \left(\mathbf{S}^T\mathbf{W}^T\mathbf{W}\mathbf{S} + \lambda\mathbf{R}^T\mathbf{R}\right)^{-1}\mathbf{S}^T\Delta v, \tag{3.6}$$

where $\mathbf{W}$ is a weighting matrix, $\mathbf{R}$ and $\lambda$ are the regularization matrix and regularization parameter, respectively, as described in the previous section. Note that assuming $\mathbf{W}^T\mathbf{W}$ as an identity weighting matrix, $\mathbf{S}^T\mathbf{W}^T\mathbf{W}\mathbf{S}$ is an approximation of the Hessian. In Bayesian theory, $\mathbf{W}$ is chosen as the inverse of the data covariance matrix and $\lambda\mathbf{R}^T\mathbf{R}$ is chosen as the inverse of the model covariance matrix. In this study, assuming uncorrelated measurements, $\mathbf{W}$ is assumed to be an identity matrix.

A proper choice of $\lambda$ can be obtained e.g., according to the Morozov's discrepancy principle criterion [Hansen, 1998]. According to this criterion, the smallest $\lambda$ is chosen as the regularization parameter which satisfies the following expression,

$$\|\psi(\Delta\sigma_\lambda) - \Delta v\|_2^2 \geq \delta_n^2, \tag{3.7}$$

where $\Delta\sigma_\lambda$ denotes the dependence of the regularization parameter $\lambda$ on the reconstruction $\Delta\sigma$ and $\delta_n$ represents the standard deviation of the measurements.

#### 3.3.1.2 Subsequent Iterations

(3.6) can be interpreted as an iterative regime initiated at a reference distribution $\sigma_{ref}$ with the corresponding measurements $v_{ref}$ such that $\Delta\sigma = \sigma - \sigma_{ref}$ and $\Delta v = v - v_{ref}$. Although, the effect of subsequent iterations is marginal, the reconstructions can be slightly improved [Soleimani and Lionheart, 2006]. The solution for $\Delta\sigma$ can be obtained using subsequent iterations as follows,

$$\sigma_{n+1} = \sigma_n + \alpha_n(\mathbf{S}_n^T\mathbf{W}^T\mathbf{W}\mathbf{S}_n + \lambda_n\mathbf{R}_n^T\mathbf{R}_n)^{-1}\mathbf{S}_n^T(v_n - v_{ref}), \tag{3.8}$$

where the resultant solution can be obtained from $\Delta\sigma = \sigma_{n+1} - \sigma_{ref}$. Here, $\alpha_n$ denotes the step length. Computation of the sensitivity matrix at each iter-

ation and finding proper step lengths and regularizations makes the iterative methods computationally demanding.

### 3.3.2 Truncated Singular Value Decomposition

By expressing SVD of $\mathbf{S}$ as $\mathbf{U}\Sigma\mathbf{V}^T$, where $\mathbf{U} = [\mathbf{u}_1, \mathbf{u}_2, \ldots, \mathbf{u}_m] \in \mathbb{R}^{m\times m}$ and $\mathbf{V} = [\mathbf{v}_1, \mathbf{v}_2, \ldots, \mathbf{v}_n] \in \mathbb{R}^{n\times n}$ are the singular vectors which form a basis for the data and the model space, respectively, and $\Sigma$ is a diagonal matrix, the diagonal entries of which are called the singular values, $\mathbf{S}^\dagger$ can be computed from $\mathbf{V}\Sigma^\dagger\mathbf{U}^T$ where $\Sigma^\dagger$ is the pseudoinverse of $\Sigma$ with every nonzero entry replaced by its reciprocal. Due to the ill-conditioning of $\mathbf{S}$, a truncation by using only the $t$ column vectors of $\mathbf{U}$ and $\mathbf{V}$ corresponding to the $t$ largest singular values is preferred to stabilize the inversion when the data are inaccurate. Therefore, the solution can be computed from,

$$\Delta\sigma = \mathbf{V}\Sigma_t^\dagger\mathbf{U}^T\Delta v \tag{3.9}$$

where the subscript $t$ defines the truncation level that determines the stability of the inversion by ignoring the $n$ – $t$ number of small singular values in $\Sigma$.

Let $\rho_1$ be the largest singular value and $\rho_k$ as the $k^{th}$ largest one, the proper selection of the truncation level $k$, can be established by choosing the maximum $k$ that satisfies the following equality [Golub and Loan, 1989],

$$SNR = 20\log_{10}\left(\frac{\Delta v_{rms}}{\delta_{rms}}\right) \geq 20\log_{10}\left(\frac{\rho_1}{\rho_k}\right) \tag{3.10}$$

where $\Delta v_{rms}$ and $\delta_{rms}$ are the root mean square of the perturbed voltage signal and the noise signal, respectively. The left hand side of the inequality is defined as the signal to noise ratio (SNR). If the noise is modeled as an additive white Gaussian noise of zero mean, $\delta_{rms}$ denotes the corresponding standard deviation.

# CHAPTER 4

# SYSTEM OPTIMIZATION

## 4.1 Introduction

The experimental MIT systems that have been built so far are designed to encircle the region of interest with fixed 16 measurement channels and the imaging quality of those are analyzed previously in various studies. However, possible other configurations have not been explored in detail so far and whether the existing 16-channel MIT systems are optimal in the sense of imaging performance or not is still an open question. This chapter addresses this problem and tries to improve the imaging performance by finding better designs. To this end, the existing systems were compared with other alternative system configurations to conclude the influence of coil orientations on the image quality [Gürsoy and Scharfetter, 2009c]. Furthermore, a deterministic algorithm was proposed to end up with optimal coil designs in a feasible amount of time based on maximizing the independent information of the measurements [Gürsoy and Scharfetter, 2009b].

## 4.2 Effect of Coil Orientations on Imaging

In MIT, the change in the magnetic field due to the conductivity perturbation is much weaker than the primary magnetic field which leads to a narrow dynamic range in the receiver channels. Therefore, much effort has been expended so far with the aim of reaching an efficient coil configuration to extend the dynamic range of the measured signal. For this purpose, flux cancellation

techniques have been extensively analyzed. However, the merits of different sensor orientations on the imaging performance have not been studied in great detail so far. Therefore, the aim is to fill the void of a systematic investigation of the coil orientations on the reconstruction quality of the designs.

To this end, a number of alternative receiver array designs with different coil orientations were suggested and the evaluation of the designs was performed based on SVD assuming that the underlying model is linear. The image resolution and variance measures were used to analyze the performance on the radial and axial axes of a cylindrical phantom and a class of quality measures, the subclasses of which are linked to these measures, i.e., spatial resolution and image uncertainty, was used to assess the overall performance of the designs. The detectability of three different local conductivity perturbations in the phantom was investigated using the reconstructed images for noisy and noise-free data.

### 4.2.1 Evaluation Criteria

#### 4.2.1.1 Image Resolution and Uncertainty

From the linear inverse theory, it is possible to obtain the theoretical resolution limits and the uncertainty of the reconstructions in terms of the sensitivity matrix. By using (3.3) and (3.4), the resolution matrix is given as follows,

$$\mathbf{R} = \mathbf{S}^{\dagger}\mathbf{S}, \tag{4.1}$$

of which the columns are called the point spread functions as they represent the response of the system due to a point source. Ideally, when the resolution is perfect, $\mathbf{R}$ is an identity matrix, however, due to the absent information that lies in the kernel of $\mathbf{S}$, $\mathbf{R}$ is significantly different from an identity matrix.

A similar relation can be written to describe the uncertainties in the model parameters. The model covariance matrix provides an estimate how the errors will propagate from the data space into the model space and can be written as,

$$\mathbf{C}_m = \left(\mathbf{S}^T\mathbf{C}_d^{-1}\mathbf{S}\right)^{-1}, \tag{4.2}$$

where $\mathbf{C}_d$ is the data covariance matrix.

Assuming that the data are uncorrelated and the data variances are normalized to unity, (4.1) and (4.2) can be expressed in terms of the SVD components,

$$\mathbf{R} = \mathbf{V}\Sigma^{\dagger}\Sigma\mathbf{V}^T \tag{4.3}$$

$$\mathbf{C}_m = \mathbf{V}\Sigma^{\dagger}\Sigma^{\dagger}\mathbf{V}^T. \tag{4.4}$$

From (4.3) and (4.5), it is clear that the resolution is simply $\mathbf{V}\mathbf{V}^T$ considering only the singular vectors corresponding to the nonzero singular values and the model covariance is the "weighted" version of the resolution matrix by the square of the associated singular values.

#### 4.2.1.2 Generalized Quality Measures

A generalized class of quality measures can be obtained using the SVD of the sensitivity matrix to serve as a basis for the evaluation [Curtis, 1999]. It is also possible to quantify the previously explained image resolution and uncertainty by selecting particular subclasses of this measure. Usually, the desired measure shall focus onto a region, e.g. a slice or a single voxel, instead of the whole conductive domain, and thus, the effect of the singular vectors that span the parameters within that region must be computed. Let $\mathbf{F} = [\mathbf{f}_1, \mathbf{f}_2, \ldots, \mathbf{f}_k] \in \mathbb{R}^{n\times k}$ be an arbitrary collection of the basis vectors for the desired region, denoted as $F$. The projection of the singular vectors onto $F$ is written as,

$$\eta_j = \left( \sum_{i=1}^{k} (\mathbf{v}_j \cdot \mathbf{f}_i)^2 \right)^{1/2} \qquad j = 1, 2, \ldots, n \tag{4.5}$$

where $\mathbf{p} = [\eta_1, \eta_2, \ldots, \eta_n]^T \in \mathbb{R}^{n\times 1}$ is defined as the projection vector. This vector denotes the effective singular vectors for $F$. For computational convenience, a natural and simple way to select the basis for $F$ is using the unit vectors oriented parallel to each of the model parameter axes and defined as follows,

$$\mathbf{F}_{ij} = \begin{cases} 1, & \text{if } i = j \\ 0, & \text{if } i \neq j \end{cases} \tag{4.6}$$

By imposing that the singular values apply a weighting to the associated singular vectors, a set of quality measures for the region $F$ can be defined as,

$$q_F(\alpha, t) = \begin{cases} \mathbf{p}^T \Sigma_t^{\alpha} \mathbf{p}, & \text{if } \alpha \geq 0 \\ \mathbf{p}^T \left(\Sigma_t^{\dagger}\right)^{|\alpha|} \mathbf{p}, & \text{if } \alpha < 0 \end{cases}, \tag{4.7}$$

where $\alpha$ can be thought as an arbitrary weighting parameter and $t$ is the truncation index. The resolution and uncertainty measures are the subset of the measure given by (4.7), with $\alpha$ taking values of 0 and -2, respectively. In these two particular cases, the resolution and uncertainty measures are equivalent to summing the diagonal elements of $\mathbf{R}$ and $\mathbf{C}_m$, respectively, which corresponds to the voxels within $F$.

The selection of the $\alpha$ parameter in (4.7) allows us to define a weighting between the resolution and the variance of the reconstructions and serves a useful base for design optimization. The $\alpha$ value determines the effect of the singular values on the imaging performance. A positive $\alpha$ value tends to increase the effect of the larger singular values than the smaller ones so that the inversion would be better constrained under low levels of SNR. Since the number of the effective singular vectors may be too little as compared to the unknown parameters, a positive weighting is usually more appropriate for the current MIT systems so that the effect of the smaller singular values are comparably reduced and the importance of the larger ones is raised.

Using (4.7), the effect of the truncation level on the quality can be expressed as,

$$(\%)\, \Delta q_F(\alpha, t) = 100 \times \left(1 - \frac{q_F(\alpha, t)}{q_F(\alpha, t_{max})}\right) \tag{4.8}$$

where $\Delta q_F$ is defined as the quality reduction in percentage due to the truncation. Considering the designs in this paper, $t_{max} = 256$ which denotes zero truncation.

### 4.2.2 Simulation Setup

Six different designs with a fixed number of coils were compared and the goal was to assess the characteristics of the receiver coil orientations in terms of

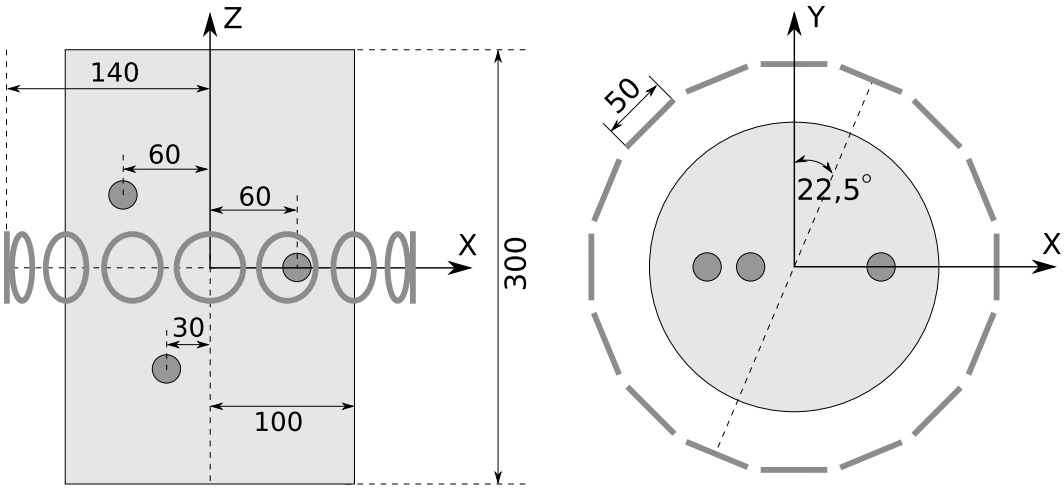


Figure 4.1: The cylindrical phantom and the positioning of the transmitter coils. The left and the right diagrams correspond to the side view and the top view. All units are given in millimetres.

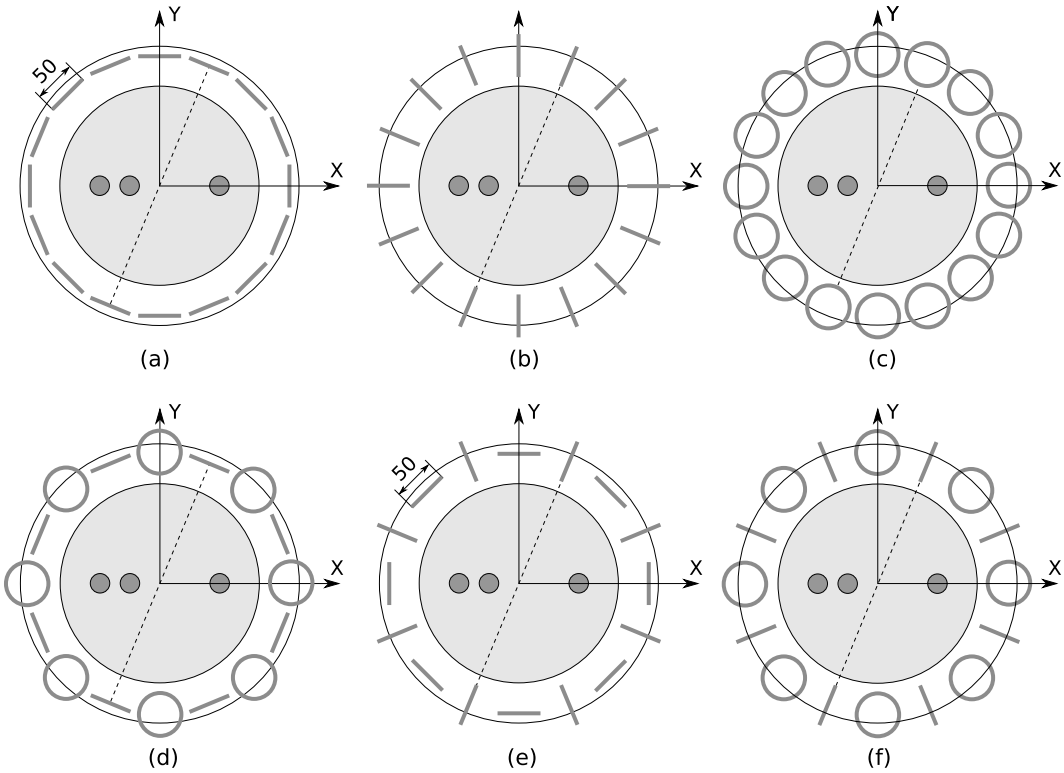


Figure 4.2: Demonstration of the receiver coil designs: (a) $D1$, (b) $D2$, (c) $D3$, (d) $D4$, (e) $D5$ and (f) $D6$.

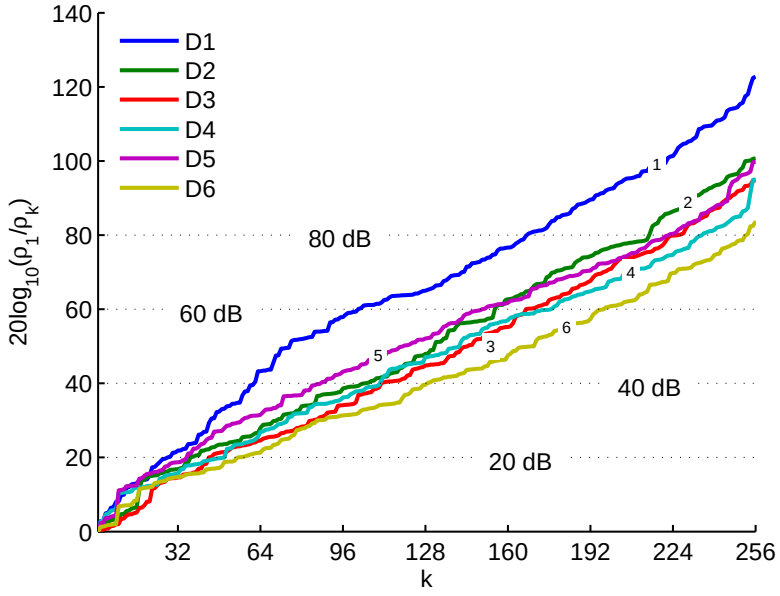


Figure 4.3: The logarithmic ratio between the first and the $k^{th}$ singular value as compared to the SNR.

the measures applied. For excitation, 16 identical solenoid transmit coils with 2.5 cm radius were used with their centers uniformly positioned on a circular ring of 14 cm radius (see, figure 4.1). 16 receiver coils with 2.5 cm radius were placed with their centers on an inner ring of 13 cm radius. The designs differed by the receiver coil orientations where the unit vector along the coil axis was allowed to point in one of the three standard cylindrical coordinate basis vectors, $\mathbf{u}_\rho$, $\mathbf{u}_\varphi$ or $\mathbf{u}_z$. The designs are shown in figure 4.2 and are denoted as $D1$ ($\mathbf{u}_\rho$), $D2$ ($\mathbf{u}_\varphi$), $D3$ ($\mathbf{u}_z$), $D4$ ($\mathbf{u}_\rho$ and $\mathbf{u}_z$ alternating), $D5$ ($\mathbf{u}_\rho$ and $\mathbf{u}_\varphi$ alternating) and $D6$ ($\mathbf{u}_\varphi$ and $\mathbf{u}_z$ alternating).

A cylindrical phantom of 10 cm radius and 30 cm height with three local spherical inhomogeneities inside was used to test the imaging performance of the designs. The inhomogeneities had comparatively small radii of 1 cm so as to reflect in the images approximately the point spread functions at the locations [-6, 0, 5], [6, 0, 0] and [-3, 0, -7] cm.

Table 4.1: Optimum truncation levels for the designs corresponding to different SNR levels. (-) means that no truncation is necessary.

| Design | 20 dB | 40 dB | 60 dB | 80 dB | 100 dB |
|---|---|---|---|---|---|
| $D1$ | 28 | 62 | 102 | 168 | 222 |
| $D2$ | 37 | 105 | 155 | 215 | 253 |
| $D3$ | 44 | 111 | 167 | 227 | – |
| $D4$ | 51 | 111 | 177 | 236 | – |
| $D5$ | 36 | 88 | 150 | 223 | – |
| $D6$ | 56 | 129 | 198 | 253 | – |

### 4.2.3 Results

The sensitivity matrices of the designs were computed using a uniform conductivity distribution within the phantom and the SVD was performed on the matrices. To determine the truncation level needed for a stable image reconstruction, the logarithmic ratios according to equation 3.10 between the first and the remaining singular values as compared to the SNR levels were examined as in figure 4.3. The obtained truncation levels for the designs corresponding to several SNR levels are given in table 4.1. The curve corresponding to *D1* ascends more steeply than for all other designs, thus reflecting a faster drop of the singular values. For instance, only 28 singular values can be effectively used for image reconstruction considering 20 dB SNR. On the other hand, the curve of *D6* ascended with a more gentle slope and the corresponding truncation index was significantly higher considering the feasible SNR levels of a typical MIT system.

For a detailed analysis, the phantom was divided into thin slices of 1 cm thickness along the z-axis. The axial resolution and uncertainty measures at 20 dB SNR level associated with each slice were computed based on (4.7) by substituting the $\alpha$ values as 0 and $-2$, respectively, and the associated curves were plotted in figure 4.4. The truncation necessary for a stable inversion was obtained from table 4.1. Since the curves are symmetric with respect to the central plane, only the curves corresponding to the positive z-axis were plotted. The slices at 5 and 7 cm on the z-axis were marked as dotted vertical lines to highlight the locations of the perturbations. The curves of *D4* and *D6* showed

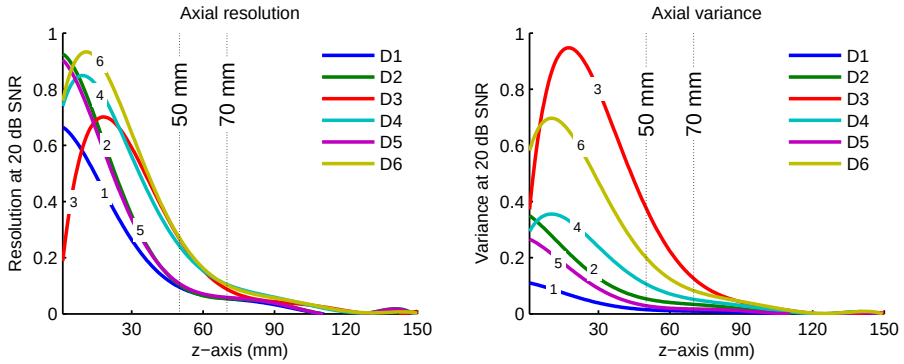


Figure 4.4: The curves of the normalized resolution and variance measures at 20 dB SNR level along the z-axis corresponding to the designs. The slices at 5 and 7 cm on the z-axis were marked as dotted vertical lines to highlight the locations of the perturbations. On the y-axes, 0 and 1 indicates the minimum and the maximum, respectively.

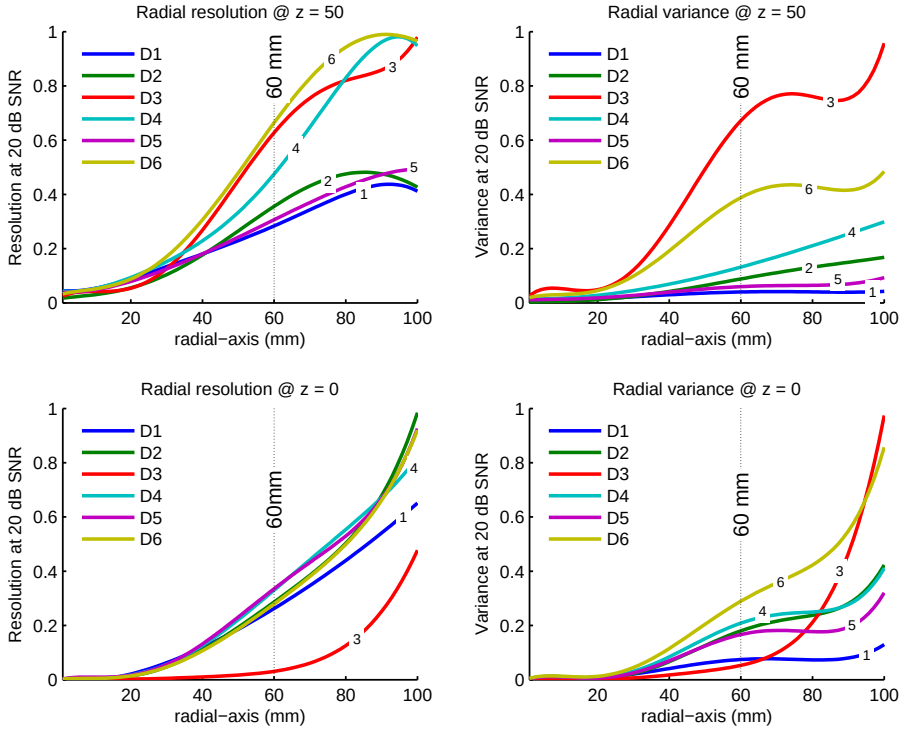


Figure 4.5: The curves of the normalized resolution and variance measures at 20 dB SNR level along the radial-axis considering different slices. The radial position at 6 cm was marked as a dotted vertical line on the radial-axis to highlight the locations of the perturbations. On the y-axes, 0 and 1 indicates the minimum and the maximum, respectively.

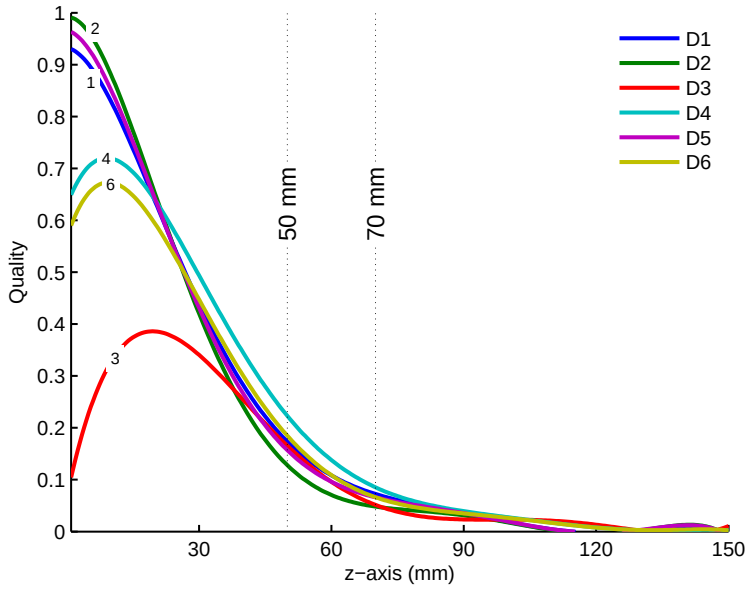


Figure 4.6: The normalized quality curves along the z-axis ($\alpha = 1$) corresponding to the designs. The slices at 5 and 7 cm on the z-axis were marked as dotted vertical lines to highlight the locations of the perturbations. On the y-axis, 0 and 1 indicates the minimum and the maximum, respectively.

the largest resolution among all designs except at the origin which represents the central slice. The peak of the curves of *D1*, *D2* and *D5* lie at the origin and they decay along the z-axis. In the variance plots, *D3* and *D6* showed the worst performance among all and *D1* was the most stable design with a low image variance.

For a radial analysis, transversal slices, i.e. at $z = 0$ and at $z = 5$ cm, were divided into tiny rings of different radii from the origin to the periphery of the slice. The thickness of the rings was selected as 1 cm. The corresponding curves of the resolution and variance measures at 20 dB SNR level along the radial-axis for two different slice positions were given in figure 4.5. The radial position at 6 cm was marked as a dotted vertical line on the radial-axis to label the location of the perturbation. *D3*, *D4* and *D6* showed better resolution in the off-central plane and considering the central plane, all designs showed comparably similar performances except *D3*, the resolution of which was very low. The plots for the slice at $z = 7$ cm showed similar curves as $z = 5$ cm and, thus, were not presented.

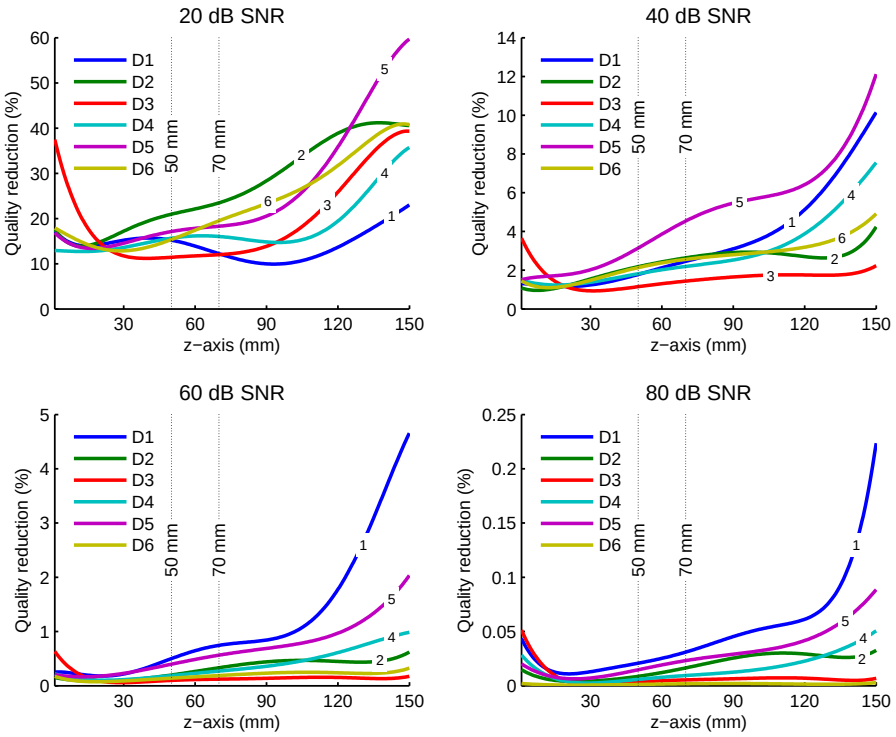


Figure 4.7: The effect of SNR on the design qualities of the designs ($\alpha = 1$). The slices at 5 and 7 cm on the z-axis were marked as dotted vertical lines to highlight the locations of the perturbation .

It is, in principle, not sufficient to investigate only the image resolution to compare the designs. For instance, some designs may show better resolution performances but the corresponding images might be unstable when the data are noisy. This shows the necessity of the overall performance measures as given in (4.7). For the demonstration, a quality measure with a unity weight ($\alpha = 1$) was considered and the curves were plotted in figure 4.6. As noted from the plots, the quality of *D1*, *D2* and *D5* was significantly weighted for the central slice due to their low image variance. *D3* showed a very poor quality especially for the central slice and *D4* and *D6* showed fairly good results. Considering the slices beyond 2 cm, *D4* outperformed the other designs.

The effect of the truncation on the design quality was analyzed according to eq13 and the plots for several SNR levels were given in figure 4.7. With 60 dB and 80 dB SNR, *D1* has the largest reduction of quality compared to the other designs. This is probably due to the large number of neglected singular

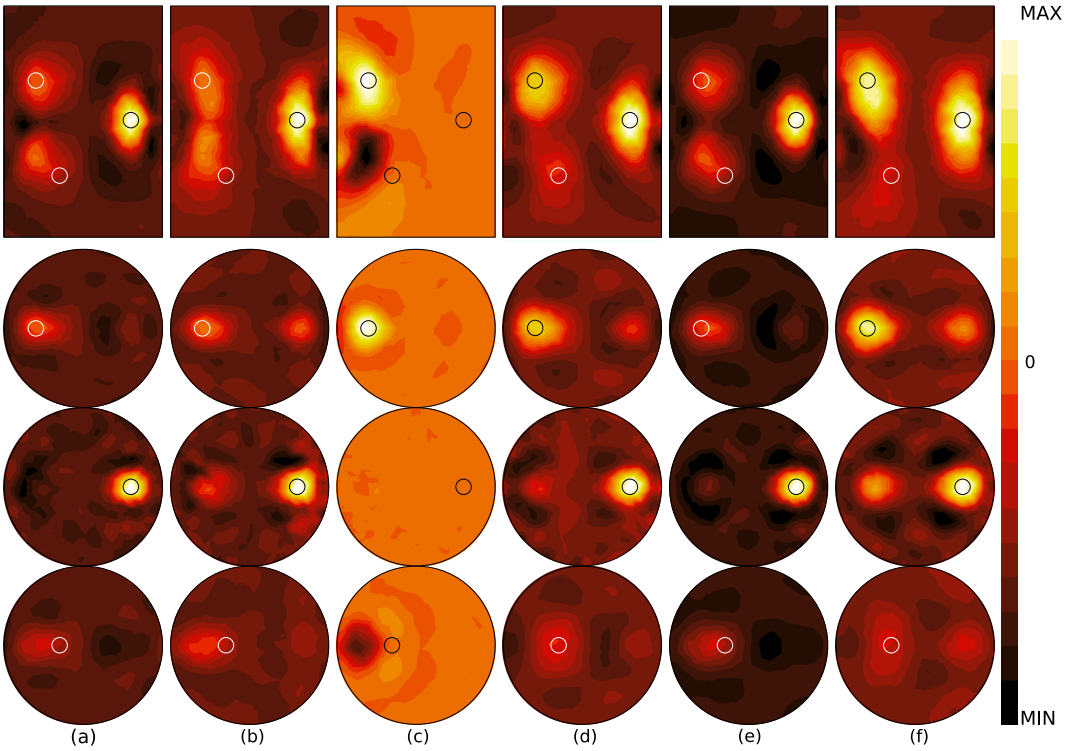


Figure 4.8: The images reconstructed from the corresponding designs using noise-free data. From left column to the right column: (a) D1, (b) D2, (c) D3, (d) D4, (e) D5 and (f) D6, respectively.

vectors. However, there is not a significant quality reduction of *D3* and *D6*. This scenario is different for low SNR levels. For 20 dB and 40 dB SNR, the qualities of *D2* and *D5*, respectively, drop rapidly, whereas, *D1* shows a moderate reduction for the associated SNR.

Reconstructed images of the designs from data without noise and with 20 dB noise are depicted for all designs in figure 4.8 and figure 4.9, respectively. The voltage data were simulated by changing the conductivity of the perturbations from 0.1 S $m^{-1}$ to 0.2 S $m^{-1}$ assuming a constant background conductivity of 0.1 S $m^{-1}$. The three transversal images were chosen to cut through the centers of the inhomogeneities. From the images, the perturbation located at [-3, 0, -7] cm was hardly recognizable and the depth sensitivity was found to be comparatively poor for all the designs. Perturbations close to the periphery appeared as bright spots but smeared out to large blobs according to their broad point spread functions. Due to the complete symmetry of the coil ring with respect to the median plane, the reconstruction algorithm could

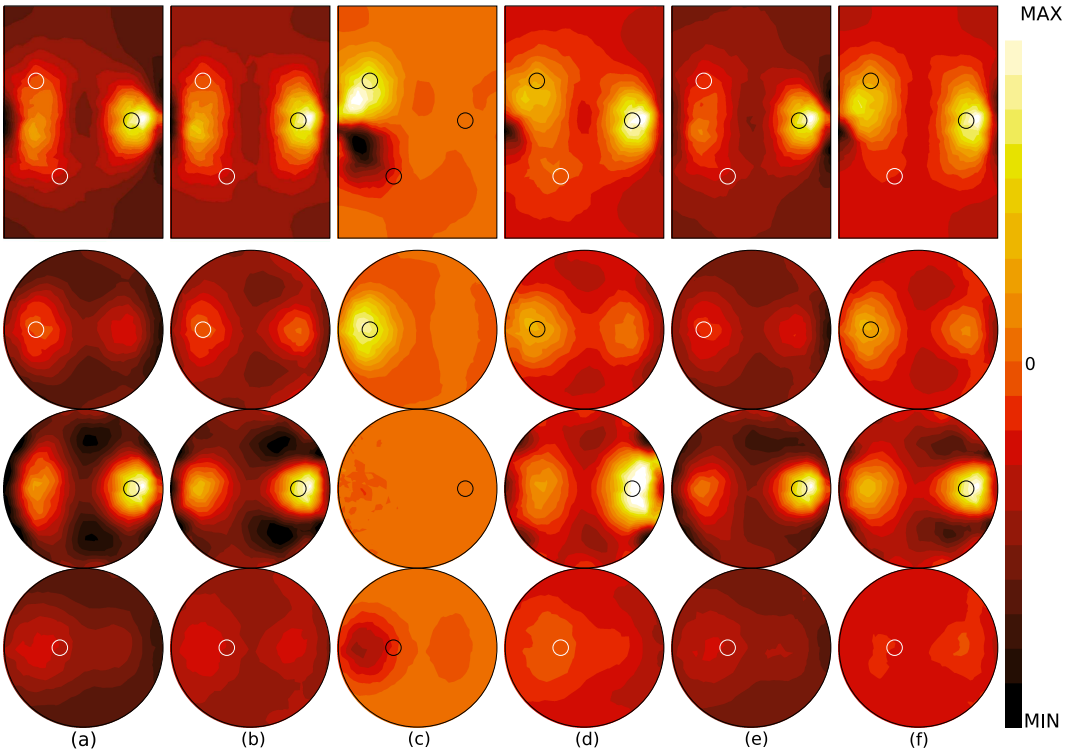


Figure 4.9: The images reconstructed from different designs using noisy data of 20 dB SNR. The truncation was applied according to table 2. From left column to the right column: (a) D1, (b) D2, (c) D3, (d) D4, (e) D5 and (f) D6, respectively.

not distinguish between the perturbations which lie symmetric with respect to the symmetry plane. Thus, each perturbation off the median plane lead to an artificial mirror image in the opposite half space and the image intensity was reduced. The mirror artifacts completely cloak the deepest perturbation in all cases. The central slice was fairly well reconstructed in almost all designs except $D3$, which has no sensitivity at all to the median plane.

### 4.2.4 Discussions

The complete resolution analysis, i.e. examining, characterizing and reporting the PSF of each voxel, is very challenging due to the large number of parameters. Usually, some measures to quantify the key features of the PSFs are desired for evaluation. A recently proposed measure was the spread of the PSF quantified by the distance at which the function reaches a percentage of its maximum value [Merwa and Scharfetter, 2007]. However, this approach is not

easily applicable for all locations due to the nonconvex and arbitrarily shaped PSFs of MIT. Thus, in this work, we suggest to use only the peak values of the PSFs for quantification. This showed results consistent with the previously used evaluation of Merwa *et al* [Merwa and Scharfetter, 2007], since the peak value was found to be strictly dependent on the spread of the function, i.e., a high peak is an indicator of good resolution and low spread. Additionally, this measure is computationally much cheaper and robust.

The stability of the reconstructions, which addresses the possible artifacts arose from propagation of data errors into the imaging domain, has not been investigated much. In this work, the evaluation was carried out by a measure which was computed from the variances of the reconstructions due to an uncorrelated data noise. A clear trade-off between the resolution and the stability was noted. For instance, a decrease in the truncation level results in a more stable inversion by removing the effect of the smallest singular values, however, leads to a poorer resolution due to the reduction of the associated singular vectors. Considering these facts, we used a quality measure by which the resolution and the stability can be weighted accordingly. The motivation behind this weighting strategy can be inferred from figure 4.5 considering the slice at $z = 5$ cm. The designs $D4$ and $D6$ show similar characteristics in terms of resolution, however, the variance curve of $D6$ shows larger uncertainty in the image domain and, thus, the overall performance of $D6$ was concluded to be poorer than $D4$. This example shows the necessity of integrated approaches to quantify the performance to be used in design optimization.

As discussed in earlier publications [Merwa and Scharfetter, 2008], $\mathbf{u}_z$ directed coils (as $D3$) have nearly the same characteristics as the vertically positioned (on end rings) planar gradiometers with their main axis pointing towards $\mathbf{u}_\rho$. Similarly, it is also possible to construct analogous gradiometer designs. For instance, considering $D2$, it is possible to build an analogous design by using horizontally positioned (side by side rings) planar gradiometers pointing in direction $\mathbf{u}_\rho$. The simulations that were not shown in the paper revealed that the zero-flow gradiometer receiver design suggested by Scharfet-

ter *et al* [Scharfetter et al., 2005], does not resemble $D1$, but produce similar images like $D3$. This is thought to be due to the comparatively larger size of the gradiometers, since the voltage induced in the ring placed far from the surface is considerably lower than the closer ring. Therefore, the designs $D2$, $D3$ and $D6$ can be fully implemented using planar gradiometers instead of coils.

The reconstruction algorithm could not distinguish between the conductivity perturbations which are placed symmetric with respect to the median plane due to the complete symmetry of the coil rings. This causes artificial mirror images in the opposite half space for the perturbations off the median plane. From figure 4.8, it was noted that the mirror artefacts were bound to be positive for the designs $D1$, $D2$ and $D5$, the coil axes of which point along the horizontal directions ($\mathbf{u}_\rho$ and $\mathbf{u}_\varphi$) and negative for $D3$ which is constructed by $\mathbf{u}_z$ oriented coils. Therefore, considering the designs $D4$, $D6$, which have both the vertically and horizontally oriented coils, the mirror artefacts were partly cancelled due to the different sign characteristics of the artefacts.

## 4.3 Optimal Coil Positioning

The previous section mainly discussed the effect of coil orientation on the imaging performance of the system by comparing several alternative designs. Although, this study provides intuitive justifications on how to design experiments, it is not feasible to compare all possible configurations in a reasonable amount of time. Therefore, in this section, a fast and deterministic optimal design strategy is presented and the resultant designs are analyzed.

### 4.3.1 Optimization Algorithm

The design strategy used aims at maximizing the degree of the independence between the rows of the sensitivity matrix in order to decrease the condition number of the Hessian matrix. This could also be interpreted as minimizing the degree of mutual information between the measurements (see, appendix).

Let the quality measure for a particular design be defined in terms of the N-dimensional angle between the rows of the sensitivity matrix as given below,

$$\alpha_{mn} = \left( \frac{\mathbf{s}_m \cdot \mathbf{s}_n}{\|\mathbf{s}_m\| \, \|\mathbf{s}_n\|} \right)^2, \tag{4.9}$$

where $\mathbf{s}_i$ corresponds to the $i^{th}$ row of the sensitivity matrix. The $\alpha$ values are simply the square of the cosines of the angles between the rows and are defined in $[0, 1]$. When $\alpha$ is closer to 1, then the row vectors are dependent. Thus, $(1 - \alpha)$ represents a quality measure. This relationship is sometimes referred to as the normalized data resolution (or information) matrix [Jackson, 1972]. The more orthogonal the vectors are, the more independent information content they provide. Based on (4.9), a quality measure for a specific receiver is given as follows,

$$Q_r = \frac{1}{KN} \sum_{k=1}^{K} \sum_{n=1}^{N} \left( 1 - \frac{\alpha_{kn} + \alpha_{nk}}{2} \right). \tag{4.10}$$

Here $N$ is the possible number of independent measurements, namely, the total number of rows in the sensitivity matrix, and $K$ is the number of different transmitters which yield the different measurements in the $k^{th}$ receiver. The outer sum is over the values of $\alpha$ for the particular receiver $r$ that the transmitters are coupled with it to form a transmit-receive pair. $Q_r$ reflects the gain of information which each receiver contributes to the information of the whole set.

Usually, the maximization of the spatial resolution in a particular region (e.g., a slice) is desired. This is possible by weighting the sensitivity matrix before the optimization procedure by multiplying all the columns of the sensitivity matrix with weights in such a way that columns corresponding to voxels in the focus region are emphasized while the remaining ones are de-emphasized. In the extreme case, all the columns of the sensitivity matrix for voxels outside the focus region are set to zero.

The applied algorithm works as follows: (1) Choose a set of receiver geometries that spans all feasible designs in a discrete manner, (2) compute the sensitivity of the whole set. If focusing to a specific region is desired, use the weighted sensitivity matrix. (3) compute the angles between all rows

associated with independent transmit-receive combinations, (4) reduce the receiver which provides the least loss of information when being removed from the remaining set. (5) Update the sensitivity matrix by deleting the rows corresponding to the discarded receiver. (6) Continue looping through these steps (2-5) until a stopping criterion is reached. In this study, the algorithm was stopped when a desired number of receivers, i.e., 16 or 32 was reached. Of course other criteria are possible, i.e., until the achievable resolution in a certain region passes a certain threshold or the algorithm could also stop if the derivative of the overall quality measure calculated at each step exceeds a certain threshold.

### 4.3.2 Simulation Setup

A cylindrical phantom (0.1 S $m^{-1}$) which has 3 local spherical inhomogeneities (0.2 S $m^{-1}$) was used for simulations (see, figure 4.10). The phantom had a radius of 10 cm and a height of 30 cm. Each inhomogeneity had a radius of 1 cm and was positioned at $[6,\ 0,\ 5]$, $[-6,\ 0,\ 0]$ and $[3,\ 0,\ -7]$ cm. The measurement data were simulated by changing the conductivity of the perturbations from 0.1 S $m^{-1}$ to 0.2 S $m^{-1}$.

Two different transmitter coil arrangements were selected for the simulations (see, figure 4.10). For convenience they will be referred to as T1 and T2. In T1, 8 uniformly positioned identical and radially oriented transmitters of 4 cm radius encircle the phantom, whereas, in T2, the number of circular transmitters was doubled and they were positioned in a zigzag pattern. The excitation current was 1 A for each transmitter and the excitation frequency was chosen as 200 kHz.

The full starting set of all feasible receiver positions is given in figure 4.11. The radius of the receiver coils was chosen as 2 cm and they encircle the phantom in 16 equidistant locations on 7 rings. A total of 112 circular receiver coils was used to initialize the design algorithm.

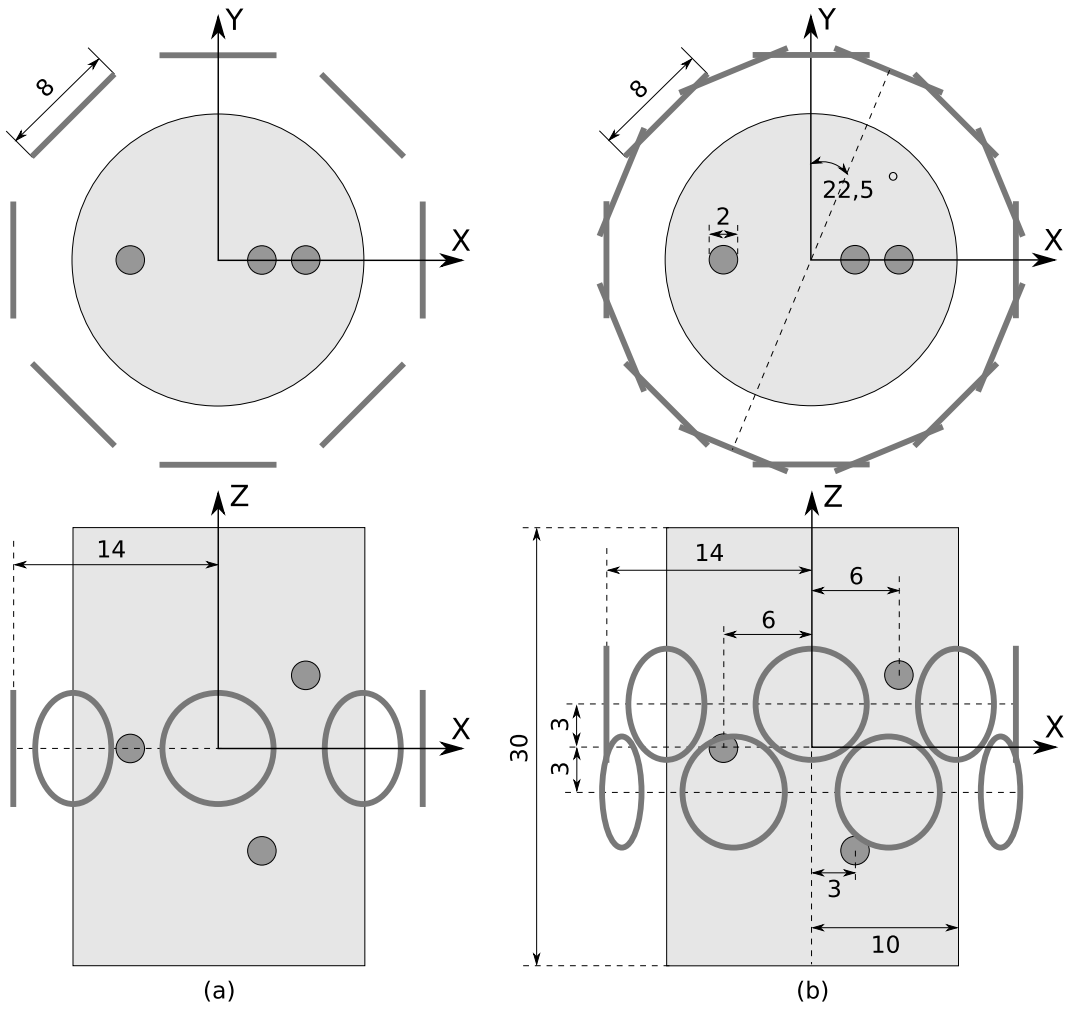


Figure 4.10: Transmitter arrangements around the cylindrical phantom (0.1 S $m^{-1}$) which has 3 local spherical inhomogeneities (0.2 S $m^{-1}$). (a) 8 flat transmitter coil geometries [T1] and (b) 16 crosswise transmitter coil geometries [T2] were used for excitation. Upper diagrams are the top views and lower ones are the side views of the simulation arrangements. All distance units are in cm.

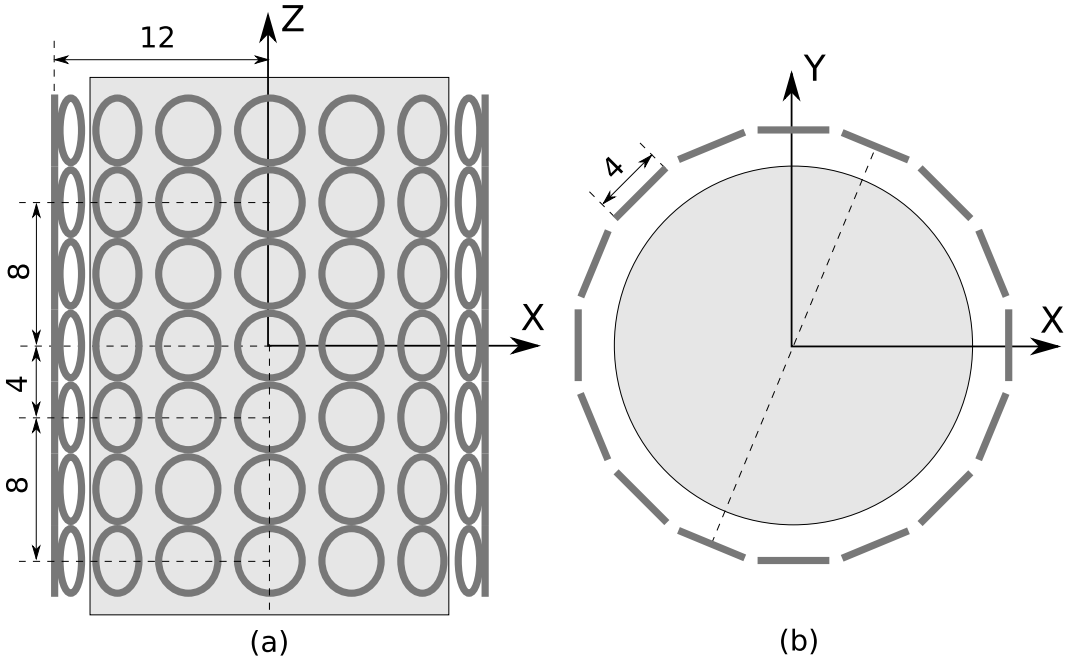


Figure 4.11: The possible receiver locations selected for the initialization of the design optimization. (a) side view and (b) top view.

### 4.3.3 Results

Three different optimization designs were realized for both T1 and T2 according to the desired improvement of the image resolution at different regions of the phantom. The first design should increase the resolution in the whole phantom and will be referred to as R1. In this case no weighting was applied to the sensitivity matrix. The other two designs should increase the resolution in the transversal slices of 3 cm thickness placed at 5 and 0 cm height on the z-axis and will be referred to as R2 and R3, respectively. In these designs, for proper focusing, all the columns of the sensitivity matrix for voxels outside the focus region are set to zero, whereas, the focused ones were not changed. The resulting optimum designs for the T1 and T2 excitations are given in Figure 4.12 and 4.14 respectively. In the figure, the dashed area at each phantom represents the region of which the information content was maximized. In R1, the optimum set of receiver coils forms two rings which are vertically 24 cm apart from each other. However, when a regional focusing was desired, the optimum set of receiver coils encircles a specific region of the selected slice in a single plane. In a second run the same strategy was applied with T2 as the

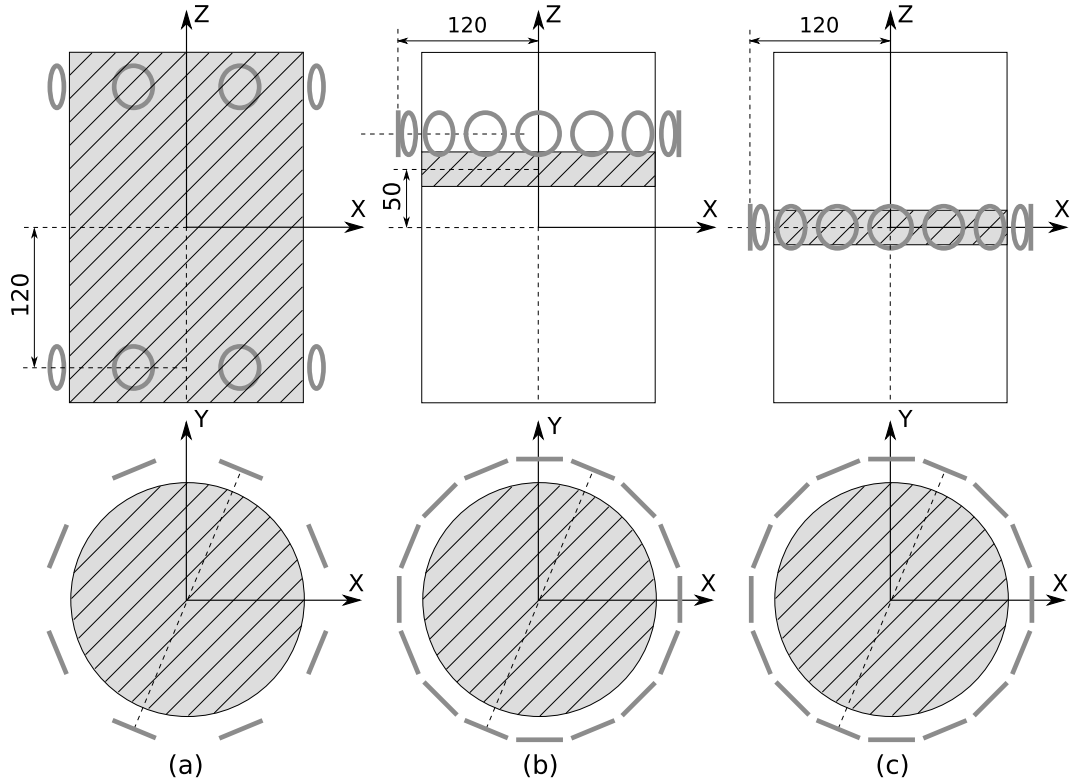


Figure 4.12: Optimum receiver designs for T1. The dashed area at each phantom represents the region of which the information content is maximized. (a) the design [R1] without focusing. (b) The design [R2] obtained by focusing to the the slice at z = 5 cm. (c) The design [R3] obtained by focusing to the central slice.

transmit configuration. Similar to R1, R2 and R3, the corresponding designs will be referred to as Ra, Rb, and Rc respectively, depending on the focus region.

When focusing onto a certain region the resolution of the images clearly increased when compared to the unfocused case (see, figure 4.13 and 4.15 by visual perception and table 4.2 quantitatively). However, this local gain of resolution was achieved at the cost of a significant resolution loss outside the focus region. Consequently only in the unfocused versions (R1 and Ra) all three perturbations could be identified simultaneously, while all other designs failed to do so. On the other hand, due to the lack of focusing, the R1 and Ra designs led to more blurry images. The reconstructions of the slice at z = 5 cm were best when using the designs R2 and Rb. However the lower half of the phantom had poor resolution. In the design R3, a spurious mirror image of

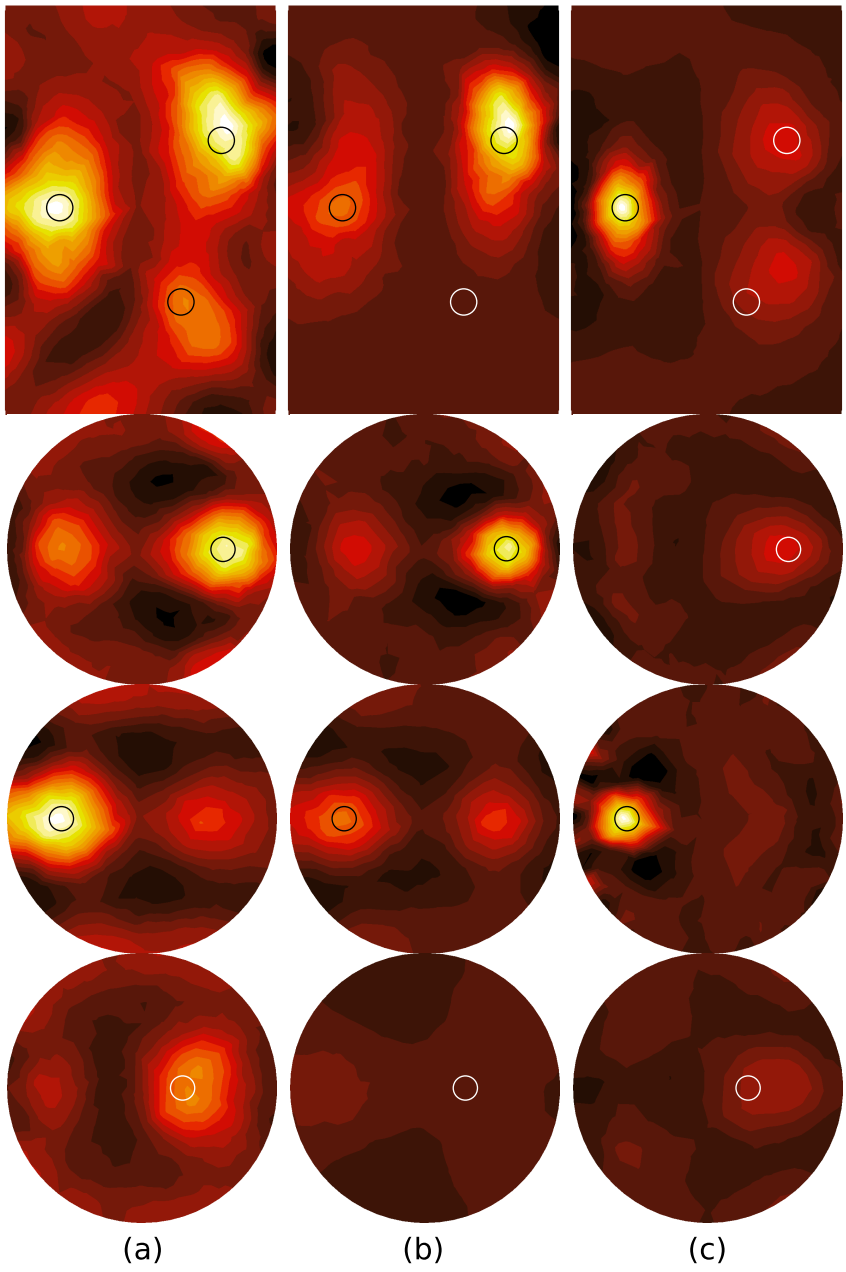


Figure 4.13: Reconstructions with the optimum receiver designs by using T1 as excitation. (a) the reconstruction obtained using R1 without focusing. (b) The reconstruction obtained using R2 which focuses to the the slice at z = 5 cm. (c) The reconstruction obtained using R3 which focuses to the central slice.

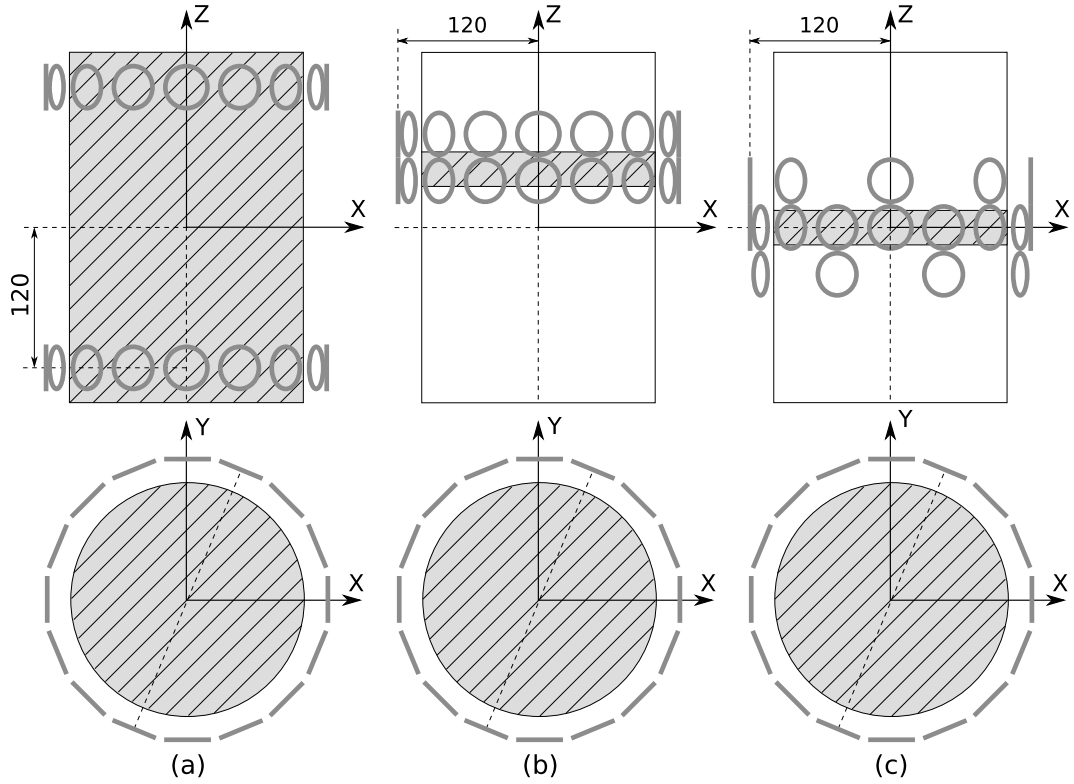


Figure 4.14: Optimum receiver designs for T2. The dashed area at each phantom represents the region of which the information content is maximized. (a) The design [Ra] without focusing. (b) The design [Rb] obtained by focusing to the the slice at z = 5 cm. (c) The design [Rc] obtained by focusing to the central slice.

the upper perturbation appeared in the lower half of the cylinder, probably because of the symmetry of the coil arrangement with respect to the median plane. The lower perturbation was possibly cloaked by that mirror artifact, due to the comparatively low sensitivity at the respective depth. When the focus should be on the central slice, the algorithm suggests to encircle the phantom with a uniform distribution of the receiver coils in the central plane of the slice, as seen in R3. Similarly, vertically paired receivers are placed in front of each transmitter coil, see the results for Rb.

The comparisons of the eigenvalues of the Hessian matrix obtained from different transmitter and receiver designs are given in figure 4.16, 4.17, and 4.18. In figure 4.16, the eigenvalues of the Hessian matrices obtained from T1 as the excitation configuration and R1, R2 and R3 as the optimized receiver designs. As expected, the design R1 tends to flatten the eigenvalue spectrum

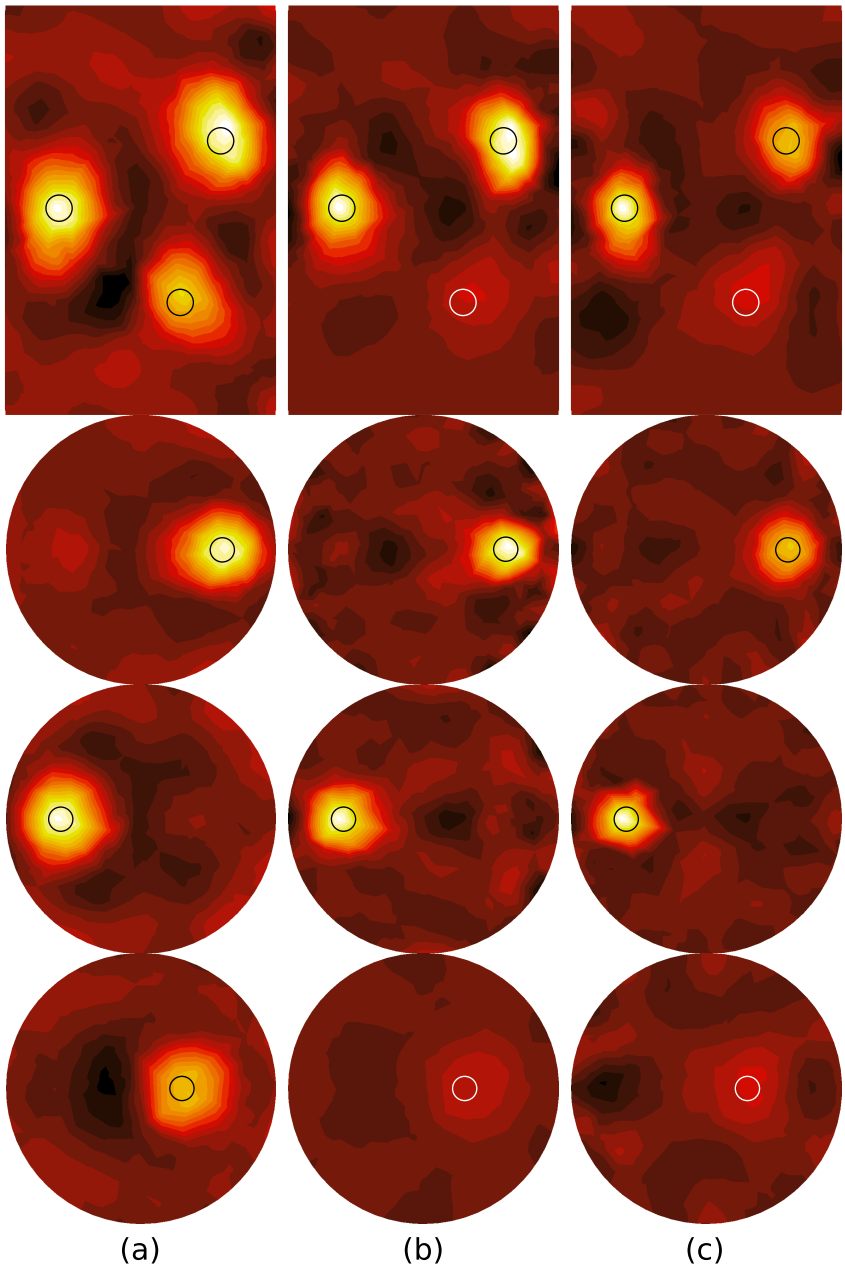


Figure 4.15: Reconstructions with the optimum receiver designs by using T2 as excitation. (a) the reconstruction obtained using Ra without focusing. (b) The reconstruction obtained using Rb which focuses to the the slice at z = 50 cm. (c) The reconstruction obtained using Rc which focuses to the central slice.

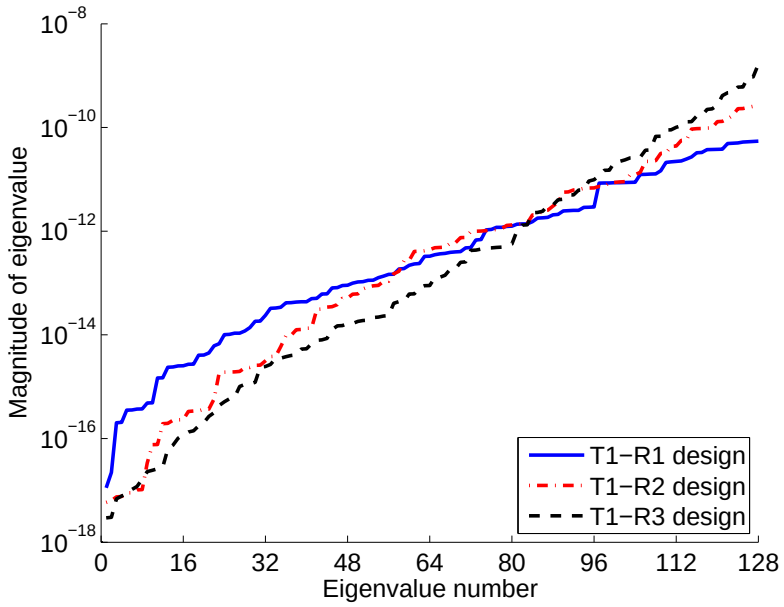


Figure 4.16: The corresponding eigenvalues of the Hessian matrices obtained from R1, R2 and R3 as receiver designs and T1 as the excitation scheme.

by increasing the small eigenvalues and reducing the larger ones. In figure 4.17, the corresponding spectrum was obtained similarly except that the Hessian was calculated only from those columns of the sensitivity matrix the voxels of which correspond to the central slice. It was noticed that the design Rc focusing onto the central slice provided the largest eigenvalues. Figure 4.18 shows that the design T2-Rc outperforms the design T1-R3 when comparing especially the smaller eigenvalues of the respective eigenvalue spectra. The quantitative results of resolution analysis was given in table 4.2. The resolution of the central slice is largest for T1-R3 and T2-Rc design compared to the remaining designs. Similarly T1-R2 and T2-Rb designs have the largest resolution at the slice positioned at z = 5 cm.

### 4.3.4 Discussions

The forward operator of MIT was linearized around a given conductivity distribution and small variations between different conductivity states were reconstructed according to the idea of difference imaging. This linearization renders possible the use of a deterministic approach. The design strategy developed

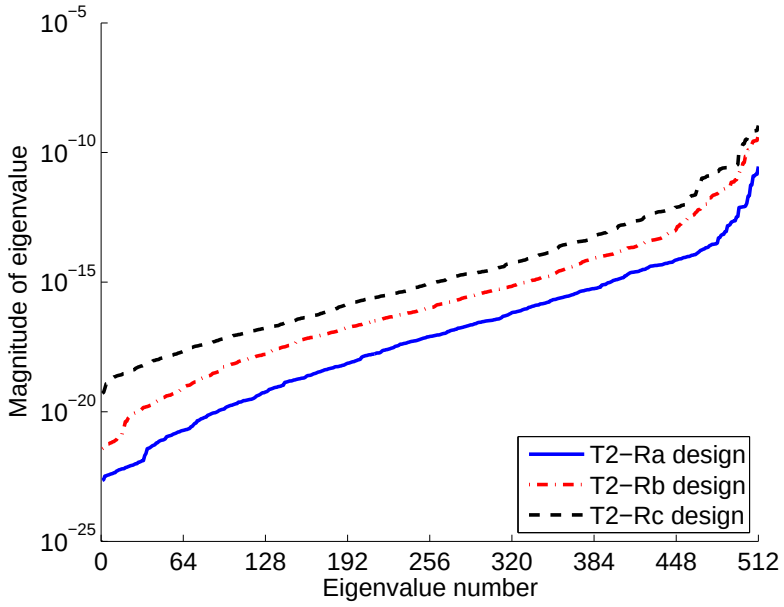


Figure 4.17: The eigenvalues of the Hessian matrices obtained from Ra, Rb and Rc as receiver designs and T2 as the excitation scheme. Only the coloumns of the sensitivity matrix which corresponds to the central slice were used for the calculation of the Hessian.

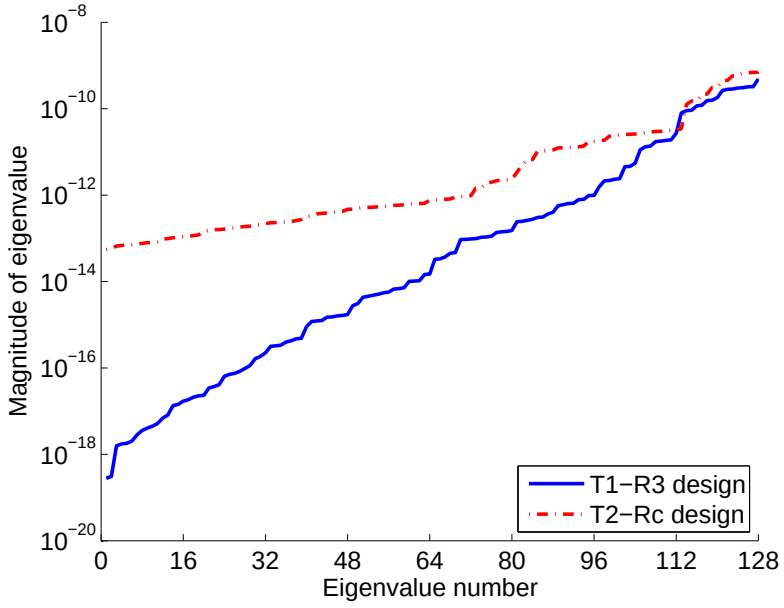


Figure 4.18: The corresponding eigenvalues of the Hessian matrices obtained from R1 and Ra as receiver designs and T1 and T2 as the excitation schemes. For convenience, only the largest 128 of 512 eigenvalues are plotted for T2-Rc design.

Table 4.2: Total resolution ($tr(\mathbf{S}^{\dagger}\mathbf{S})$) of (A) the central slice and (B) the slice at z = 5 $cm$ for the corresponding designs.

| | (A) | (B) |
|---|---|---|
| $T1 - R1$ | $0.018 \cdot 10^{-9}$ | $0.109 \cdot 10^{-9}$ |
| $T1 - R2$ | $0.170 \cdot 10^{-9}$ | $1.210 \cdot 10^{-9}$ |
| $T1 - R3$ | $3.730 \cdot 10^{-9}$ | $0.743 \cdot 10^{-9}$ |
| $T2 - Ra$ | $0.106 \cdot 10^{-9}$ | $0.341 \cdot 10^{-9}$ |
| $T2 - Rb$ | $2.691 \cdot 10^{-9}$ | $6.184 \cdot 10^{-9}$ |
| $T2 - Rc$ | $8.071 \cdot 10^{-9}$ | $3.425 \cdot 10^{-9}$ |

was based on the calculation of the sensitivity matrix. Therefore no voltage data simulation or noise considerations were needed to obtain optimal designs. MIT designs which are currently used in existing hardware were evaluated and it was shown that better designs can be achieved for different excitation and receiver patterns.

The solution of the inverse problem is a time consuming process. Even in the linearized case, the optimum experimental design approaches requires a vast number of forward problem solutions. Thus, it is essential to reduce the possible set of solutions to a computationally feasible set. The resulting designs are, accordingly, assumed to be an optimum subset of the initial set of geometries. This method does not guarantee the global optimum because of the practical infeasibility of evaluating all possible combinations of the whole set. However, the results showed that it is possible to find an optimal setup for some practical experiments.

The possibility of "regionally focused" MIT was demonstrated. This strategy increases the image resolution in a particular region at the cost of other regions' resolution. As to the knowledge of the authors, designs which focus on a specific slice have not yet been described quantitatively in much detail. The reason may be that intuition suggests to place the receivers on a ring encircling the body on a transverse plane as closely as possible to the slice which should be investigated. This assumption is possibly the heritage of the 2D EIT imaging and was taken as a standard for MIT designs. Although it was previously

found that the resolution near the receivers is higher compared to far regions, it is unclear whether the currently used designs focus on a particular region or not.

When the increase in the resolution of the central slice is desired, the optimal receiver locations which were suggested by our algorithm are intuitive in that sense that they lead to a concentration of coils close to the desired slice of the body with a fairly equidistant spacing. However the more the desired slice is far away from the transmitter plane, the receiver locations are not chosen as the closest locations to that slice, but, a bit in opposite direction with respect to transmitter plane (i.e., see, figure 4.12-b). In addition, the results also clearly emphasize the poor resolution in regions outside the focus volume. It was also noted that the solutions with a fair overall resolution cannot be found unless the coils are also spread over a wider range in the z-direction.

## 4.4 Conclusion

A number of receiver array designs with different coil orientations were compared with the existing configuration and SVD was used to serve as a basis for the analysis. It was found that the proper choice of the coil orientations significantly influences the number of usable singular vectors; thus, the stability of image reconstruction, although the effect of increased stability on the quality of the reconstructed images was not of paramount importance due to the reduced independent information content of the associated singular vectors. Each design has its own merits and shortcomings for different imaging regions and for different SNR levels, nevertheless, considering overall characteristics, *D1*, *D2* and *D5* found to be more focused to the median plane with high resolution and low image uncertainty. For the off-median regions, *D4* was found to be moderately better among others considering the practical noise levels of MIT, i.e., 20 to 40 dB.

Additionally, a deterministic algorithm was proposed to end up with optimal coil designs. By examining the singular values of the resultant designs, it was found that the algorithm tends to increase the smaller singular values

of the spectra in order to balance the amount of information coming from the imaging domain. The algorithm provides a better conditioned relationship between the model and data parameters considering the systems having low to moderate levels of SNR. However, the design suggested by the algorithm is not suitable for systems for those having extremely large SNR levels, because, in that case most of the smallest singular values are ignored and the largest singular values gain importance over the smallest ones.

# CHAPTER 5

# ARTIFACT REDUCTION

## 5.1 Introduction

As described in previous Chapters, MIT tries to image the electrical properties of a medium under investigation using noncontact measurements. Although the idea has being successfully used for numerous industrial applications such as for surveying the rocks surrounding a borehole [Kaufman and Keller, 1989, Kaufman and Dashevsky, 2003, Wait, 1982], to detect flaws in materials [Hellier, 2001] or for crosssectional imaging of pipes in industry [Peyton et al., 1996, Ma et al., 2006, 2008, Soleimani et al., 2008], the use for medical applications has just recently came under investigation [Al-Zeibak and Saunders, 1993] and the characteristics of the device for clinical trials is not sufficient yet. This is presumably partly due to the modeling inaccuracies of the human body and this Chapter addresses some of the fundamental issues like the body movements during data acquisition [Gürsoy and Scharfetter, 2009a] and anisotropic modeling of the tissues [Gürsoy and Scharfetter, submitted] that must be tackled in order to have the modality as a successfull diagnostic tool to be used for medical applications.

## 5.2 Movement Effects

The imaging approaches so far have relied on stable models such that the forward and inverse models are placed at the same location. However, in real life applications, the patient can move inside the tomograph due to respiration or

due to other random factors. Thus, this section summarizes the issue of patient's movement during data acquisition in detail and proposes some solutions to compensate this effect.

The same problem exists in electrical impedance tomography (EIT) [Zhang and Patterson, 2005]. In EIT, the sensors are attached to the surface and this automatically roughly maintains the relative position of the body to the sensors. However, in MIT the effect is found to be more dominant on the surface of the body because the sensors are usually fixed in space and a slight shift of the body can cause a significant position change with respect to the coils.

A simulation study was conducted to see the effects of the movements in a spectroscopic 16 channel MIT system [Scharfetter et al., 2008]. To model the movement effects, the position and shape of the body was modified with respect to a reference model and spherical inhomogeneities inside the cylindrical phantom were imaged for both state and frequency differential MIT. The simulations were also conducted for 20 dB SNR level to test the stability of the imaging. To overcome the movement effect, possible pre-processing and post-processing solutions based on a filtering strategy were discussed.

### 5.2.1 Simulation Setup

A cylindrical phantom (0.1 S $m^{-1}$) which has 4 spherical inhomogeneities (0.2 S $m^{-1}$) was used for simulations and illustrated in figure 5.1. The phantom had a radius of 10 cm and a height of 20 cm. The inner perturbations had a radius of 2 cm and were positioned at $[-6,\ 0,\ 0]$, $[6,\ 0,\ 0]$, $[0,\ 6,\ 0]$ and $[0,\ -6,\ 0]$ cm. The transmitter and receiver coil pairs encircle the phantom positioned in a zig-zag arrangement. The two coils in front of a transmitter were connected in counterphase to form a gradiometer. The reference data were simulated with the conductivity of the spheres set to 0.1 S $m^{-1}$, the same as the background. The voltage data were simulated with the conductivity of the spheres raised to 0.2 S $m^{-1}$, as if the spheres were dispersive and that the second voltage set had been gathered at a higher frequency.

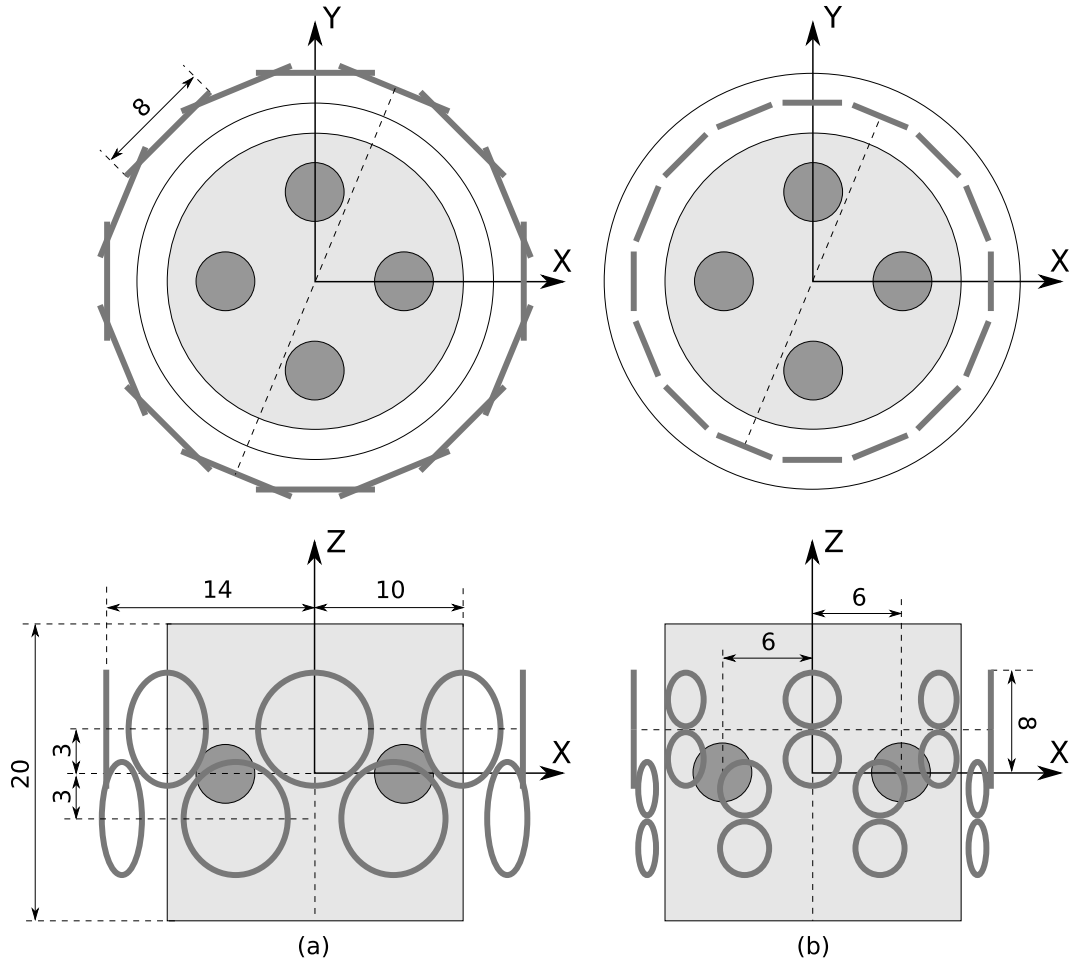


Figure 5.1: Simulation arrangement for solving the inverse problem and generating simulated voltage data: (a) transmitter setup, (b) receiver setup. All measures are in cm.

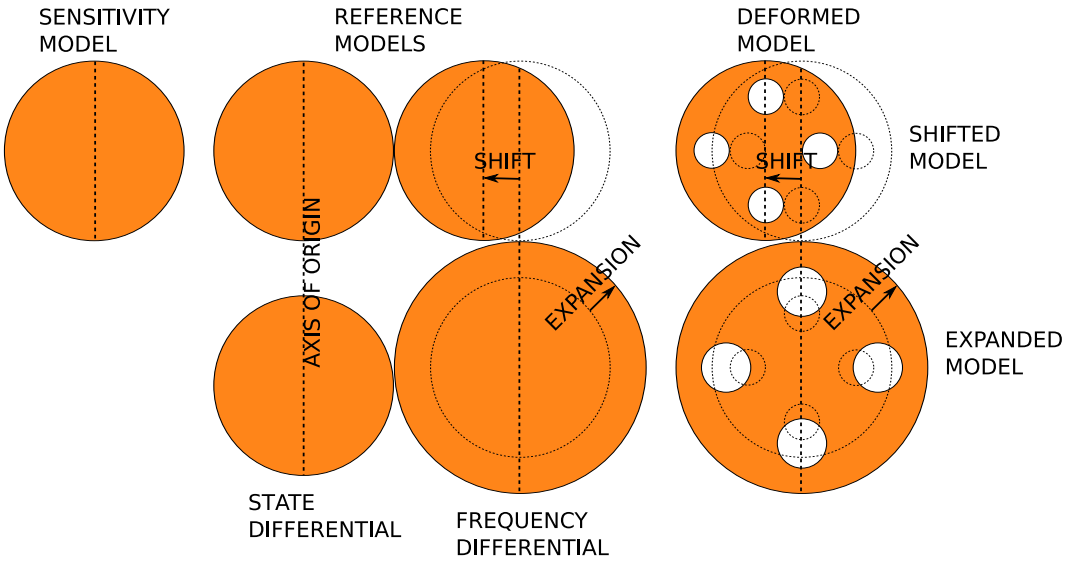


Figure 5.2: Modelling of body movements. Shifts from the original position were chosen as 2 and 4 mm which corresponds to 10% and 20% change in the distance between the surface of the phantom and the receivers. All movements are assumed to be on transversal plane

The body movement was simulated both as a shift (along -x direction from the reference position) to model the unexpected movements and as a uniform radial expansion to model the respiration artifacts and illustrated in figure 5.2. 2 mm and 4 mm of shifts/expansions were chosen which corresponds to 10% and 20% change in the distance between the surface of the phantom and the receivers. In state differential simulations, the reference and voltage data were assumed to be taken at different times, which may result in geometrical inconsistencies between the states. Therefore, the reference data were simulated from the original configuration and the voltage data were obtained from the geometrically distorted model. However, in frequency differential simulations, the reference and voltage data were assumed to be taken simultaneously, as a snapshot. Thus, the reference data were also taken from the homogenous but distorted model. The sensitivity matrix had been computed for the original state assuming a zero information about the movement/distortion.

### 5.2.2 Evaluation Criteria

The image quality was quantitatively compared by calculation of the Pearson product-moment correction coefficient (PMCC) between the images with and without the geometrical distorsion for different types of body movement to indicate the strength of linear relationship between them. PMCC for the two reconstructions $\Delta\sigma_1$ and $\Delta\sigma_2$ is defined as,

$$PMCC_{\Delta\sigma_1,\Delta\sigma_2} = \frac{\sum x_i y_i - n\bar{x}\bar{y}}{(n-1)s_x s_y}, \tag{5.1}$$

where $\bar{x}$ and $\bar{y}$ are the sample means of $\Delta\sigma_1$ and $\Delta\sigma_2$ , $s_x$ and $s_y$ are the sample standard deviations of $\Delta\sigma_1$ and $\Delta\sigma_2$ and $n$ is the number of voxels in the inverse mesh.

### 5.2.3 Filtering Strategy

It was observed that the image obtained in the presence of movement is a linear combination of the movement artifacts and the undistorted image. Therefore, if the geometrical distortions of the body surface is measured in terms of expansion and shifts/rotation, the geometrical modelling errors can be filtered out by subtracting the simulated data of the distorted uniform model from the raw data before the image reconstruction process (pre-filtering). It is also possible to filter out the effects after the image reconstruction process (post-filtering) similarly by subtracting the images obtained by using the simulated data and real data, however, the latter one is more time consuming and will only be used for visualizing/understanding the filter behaviour. For practical purposes, pre-filtering is more suitable since it requires only one inversion instead of two inversions.

### 5.2.4 Results

The images were reconstructed for different types of movements using the simulation arrangement which is given in figure 5.1. State and frequency differential MIT reconstructions for different degrees of shift in $x$-direction and radial expansion were given on figure 5.3. The colorbar is the same for all

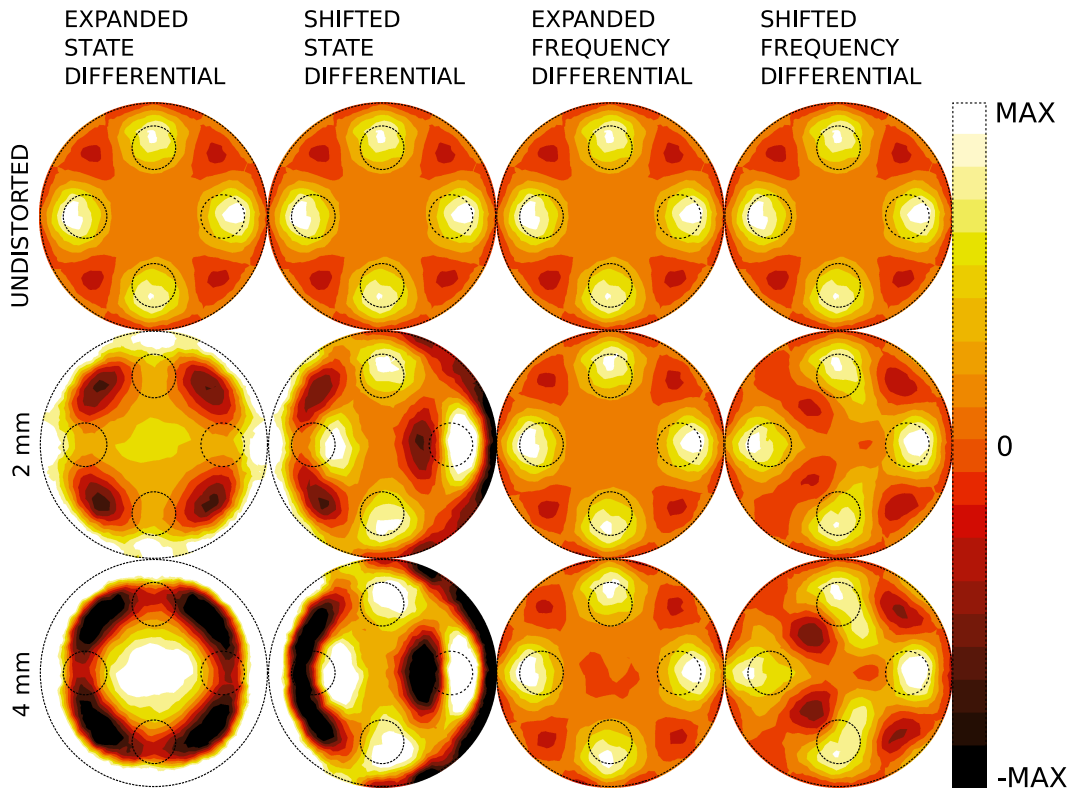


Figure 5.3: Noise free reconstructions.

images and *max* denotes the maximum conductivity value of the undistorted reconstructions when no shift or expansion was present (upper row). For the state differential images, strong positive and negative artifacts arose at those surface regions which experience the largest change of normal distance with respect to the coils. This artifact on the surface propagated towards the center in an oscillatory manner. In frequency differential images, the perturbations appear partly displaced and ghosts appear/shift especially near/towards the central region. However, no considerable artifacts were noted in the images of radially expanded models. While in the frequency differential images, the perturbations can be identified even at comparatively strong distorsions, this is hardly possible in the state differential images.

The simulations with 20 dB noise added to the data are presented in figure 5.4. With noisy data, excessive values of conductivity were observed on the surfaces of the phantom in the state differential images and the artifacts propagated towards the center in an oscillatory manner similarly. While this artifact heavily corrupted the state differential images, the frequency differental images

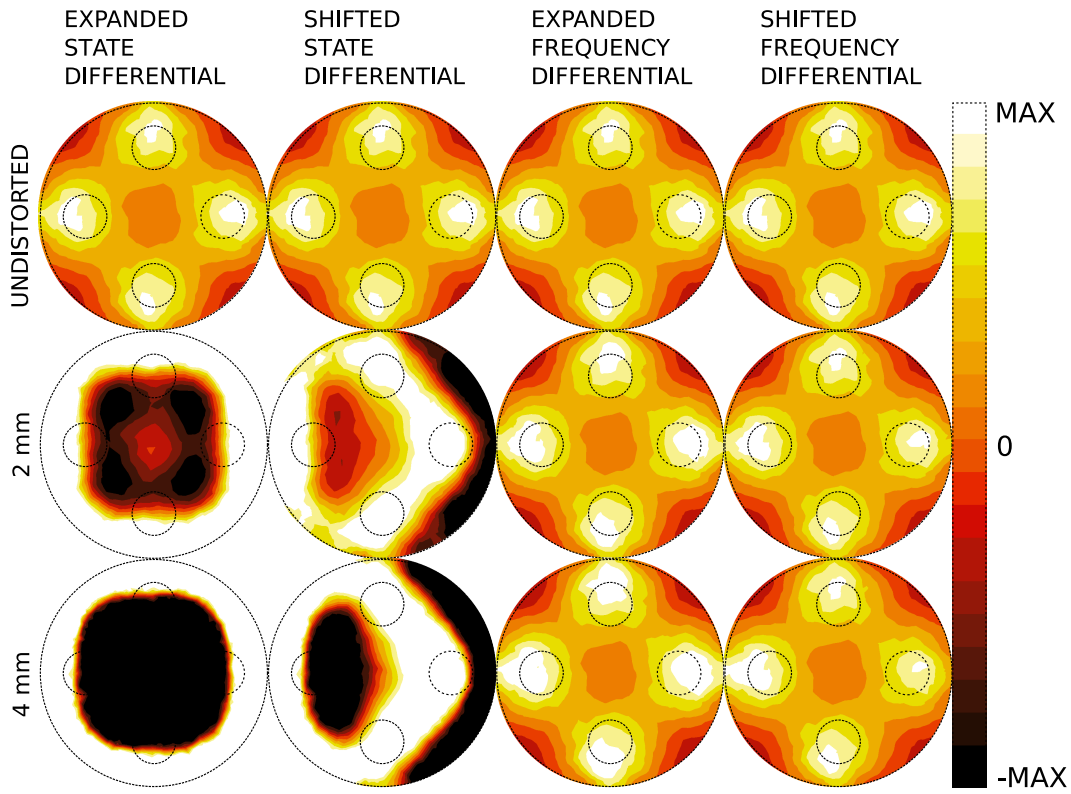


Figure 5.4: Reconstructions with 20 dB noise.

were more stable and the perturbations were identified clearly. In addition, in frequency differential images, no unsymmetrycal artifacts due to the movement were noticed.

The inversion reconstructs the geometrical distortions as well as the internal inhomogeneities. However, the high reconstructed conductivity values near the surface are dominating depending on the fact that the resolution is getting low in central regions. The oscillatory behaviour and ghosts in images are expected and caused by the *sinc* like point spread functions [Merwa and Scharfetter, 2007].

The PMCC between the undistorted image and the images which were obtained with different types of movements during data acquisition are plotted in figure 5.5. The frequency differential images were significantly higher correlated than the state differential images. A moderate almost linear decay of PMCC for up to 6 mm of shifts (or change of shape) was observed in the frequency differential case. However, in the state differential case, there is a strong approximately exponential decay of the PMCC already at small

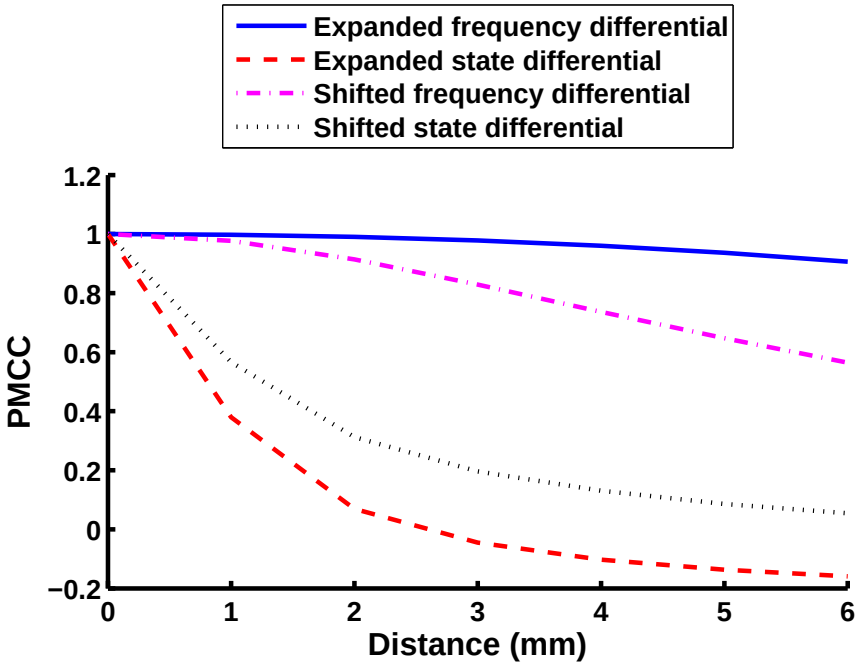


Figure 5.5: PMCC between the undistorted image and the images which were obtained with different types of movements during data acquisition.

distorsions.

It was observed that the image obtained in the presence of movement is a linear combination of the movement artifacts and the undistorted image. Therefore, if the exact position and the shape of the model during data acquisition is known, it may be possible to compensate the movement artifacts to some degree. By using the surface information, simulating the movement effect using a uniform phantom and subtracting this from the reconstructed image would remove the movement artifacts as demonstrated in figure 5.6.

### 5.2.5 Discussions

In frequency differential MIT, the data acquisition for different states is done simultaneously. This is accomplished by excitation of the body with two or more different frequencies at the same time. On the other hand in state differential MIT, the measurements between different states are taken at different times. Naturally, it is more probable to observe unwanted changes of the shape and position of the body between the states. Simulations confirmed

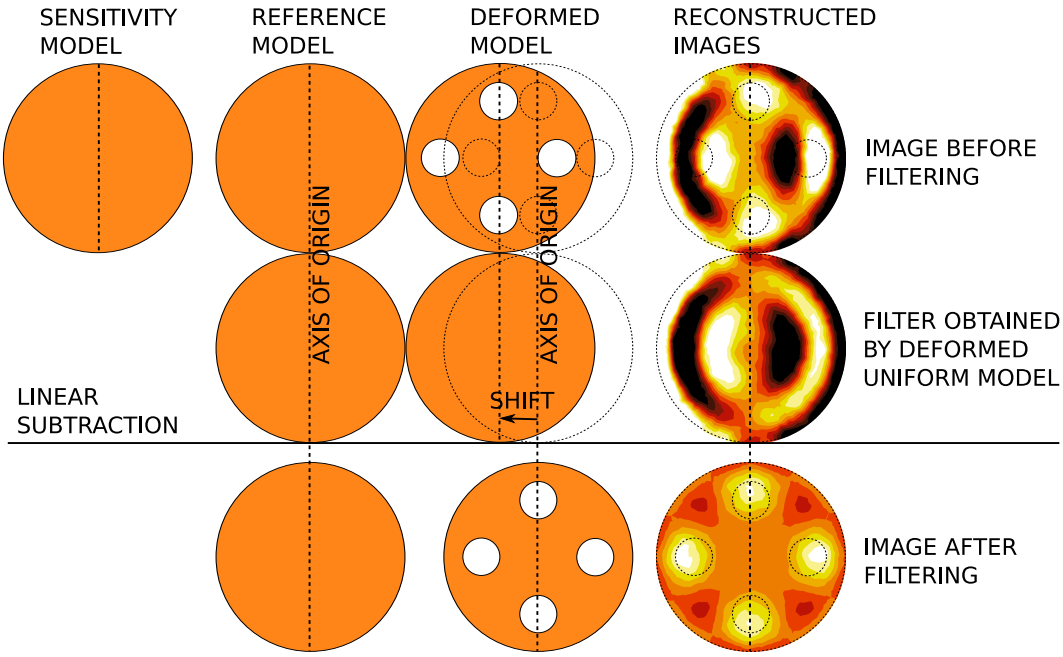


Figure 5.6: Illustration of the filtering strategy used to remove movement artifacts.

that in state differential MIT, usually the reconstructed images are either very poor or totally corrupted when body movement is present, however, frequency differential MIT is more stable to body movement effects.

In EIT, a similar discussion concerning movement effects was done [Zhang and Patterson, 2005]. However, because of the static nature of the receivers, in MIT, this movement effect is expected to be much stronger than EIT and it is presumably one of the major problems in MIT, specifically for chest imaging.

Artifacts due to the movements can be filtered out if the surface boundary is known during data acquisition. As demonstrated in figure 5.6, a linear subtraction in the image domain gives satisfactory images. Similarly, one can do the same process in the voltage data before reconstruction by subtracting the simulated data from the actual data when the uniform phantom is moved. To monitor the movement, one possibility is to use a camera system working synchronized with the data acquisition system. Similarly, cheaper solutions like ultrasonic distance sensors may also be used.

The results indicate that frequency differential MIT is more promising, especially for chest applications. However, it should be remarked that this analysis is valid only for local inhomogeneities in a non-dispersive background.

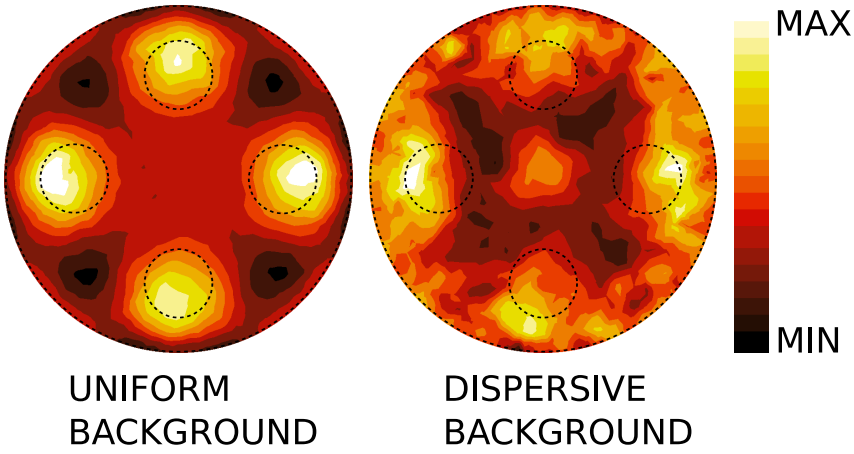


Figure 5.7: The frequency differential images obtained by assigning the (left) same and (right) different conductivity values to the background for seperate states of data simulation.

Preliminary results with realistically simulated respiration data, however, yield comparatively poor images. The reason may be the fact that in frequency differential MIT the electrical properties of the background also change between the states and the inversion algorithms so far developed have not been tested with data from object with a dispersive background. An illustration of this drawback is given in figure 5.7. The voltage data for both images was simulated by changing the conductivity of the spherical perturbations from 0.1 S $m^{-1}$ to 0.2 S $m^{-1}$. A constant background conductivity of 0.1 S $m^{-1}$ was assigned to the left phantom. In contrast, the right phantom was modelled to have a dispersive background (a conductivity change of the background from 0.1 S $m^{-1}$ to 0.15 S $m^{-1}$ between states with the same change of the perturbations). The resulting resonstructions show the incapability of the linearized inversion algorithm due to the dispersive medium and needs further analysis.

This study considers only the movement of the body as a whole and does not consider the individual movements of interior inhomogeneities. The latter would be the case when the heart and lungs moved in different directions and their shape changed independently during respiration/heartbeat cycles. The proposed solutions based on pre/post-filtering which rely on a measurement of the position of the surface of the body with respect to the coils still cannot solve the latter problem. Future work should aim at modeling and simulating

all these movements and search for possible solutions to reduce the image artifacts.

## 5.3 Modeling Anisotropy

Another modeling issue that has not been investigated so far is the effect of anisotropic tissues on the reconstructed images. The previous studies have all relied on models having an isotropic distribution of conductivity, although, the human body has a highly heterogeneous structure with partially anisotropic properties [Rigaud et al., 1996]. The conductivity of the sceletal muscle in longitudinal direction is greater than the transverse component. Similarly, the chest muscles that cover the ribs show up anisotropy in the tangential direction to the skin. Brain tissues, especially the white matter, exhibit anisotropy because of their aligned fiber structures. Furthermore, anisotropy may occur in some pathological conditions, and thus, whether the conventional modeling approaches used so far are appropriate or not for clinical applications is still an open and interesting question.

To this end, we performed a simulation study to investigate (1) the feasibility of imaging anisotropic targets within an isotropic medium and (2) the influence of anisotropic regions on the reconstruction of isotropic targets. The first case is important for imaging of the anomalies that have anisotropic characteristics and the latter becomes particularly important for imaging of the physiological fluidic changes in lungs considering anisotropic muscle tissues. An anisotropic solver based on the singular value decomposition (SVD) of the sensitivity matrix was used to achieve conductivity tensor images and the tensor images were compared with the images obtained from isotropic solvers.

### 5.3.1 Anisotropy Tensor Imaging

At first, the forward and inverse problems must be formulated considering anisotropy within the conducting body. Representing the electric anisotropic

and nonmagnetic media as follows,

$$\hat{\sigma} = \begin{pmatrix} \sigma_{xx} & \sigma_{xy} & \sigma_{xz} \\ \sigma_{xy} & \sigma_{yy} & \sigma_{yz} \\ \sigma_{xz} & \sigma_{yz} & \sigma_{zz} \end{pmatrix}, \hat{\epsilon} = \epsilon \begin{pmatrix} 1 & 0 & 0 \\ 0 & 1 & 0 \\ 0 & 0 & 1 \end{pmatrix}, \mu = \mu_0 \tag{5.2}$$

where $\hat{\sigma}$, $\hat{\epsilon}$ and $\mu$ denotes the electrical conductivity, electrical permittivity and magnetic permeability of the domain $\Omega$. For simplicity, the body was chosen as electric anisotropic by choosing the permittivity tensor as a diagonal matrix. In this tensor notation, the forward relationships defined by the potential field equations, (2.12) and (2.13), remain unchanged unless $\hat{\kappa} = \hat{\sigma} + jw\epsilon$ acts only on the function at its right. By using a symmetric tensor matrix to represent anisotropy, the parameters that we aim to reconstruct are increased at most six times. The sensitivities of the measurements to each tensor component were approximated for each voxel by using similarly from (3.4) where $\Delta\sigma$ is now a tensor, the nonzero component of which denotes the conductivity perturbation of a single tensor component from a reference distribution. Assuming admissible conductivity deviations, a system of linear equations can again be formed and the solutions can be obtained using the methods that were described previously.

### 5.3.2 Simulation Setup

The simulations were realized using the coil configuration of the Mk2 Graz 16 channel MIT system [Scharfetter et al., 2008]. A detailed illustration of the system is given in figure 5.8. The transmitter and receiver coil pairs encircle the phantom positioned in a zigzag arrangement. The radii of the transmitters and receiver coils are 4 cm and 2 cm, respectively. The two coils in front of a transmitter were connected in counterphase to form a gradiometer.

Two cylindrical phantoms of radius 10 cm and height 25 cm with different anisotropic electrical properties were used as depicted in figure 5.9. The first phantom has an isotropic background conductivity with two different anisotropic anomalies inside. The anomalies were modeled as two spherical inhomogeneties of 3 cm diameter located at [6, 0, 0] cm and [0, 6, 0] cm. The

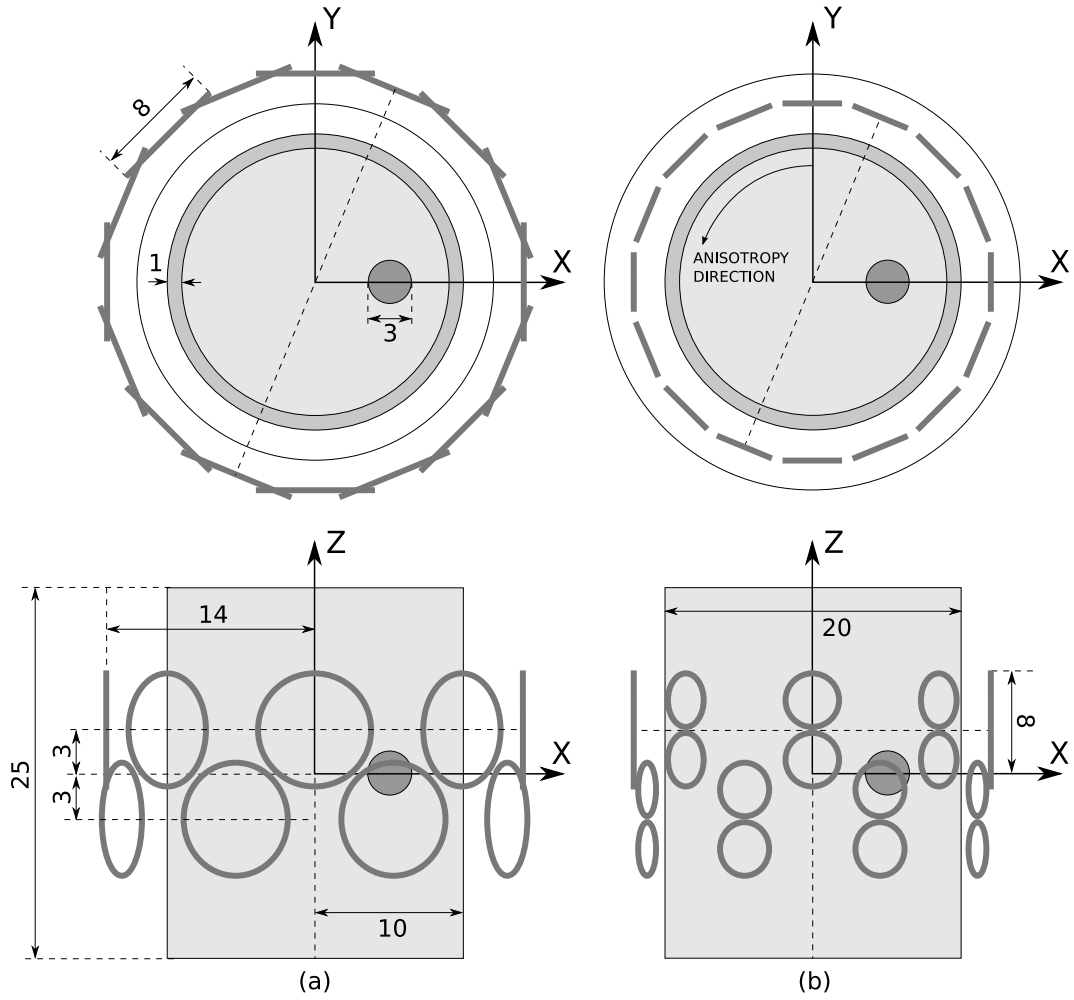


Figure 5.8: Simulation setup.

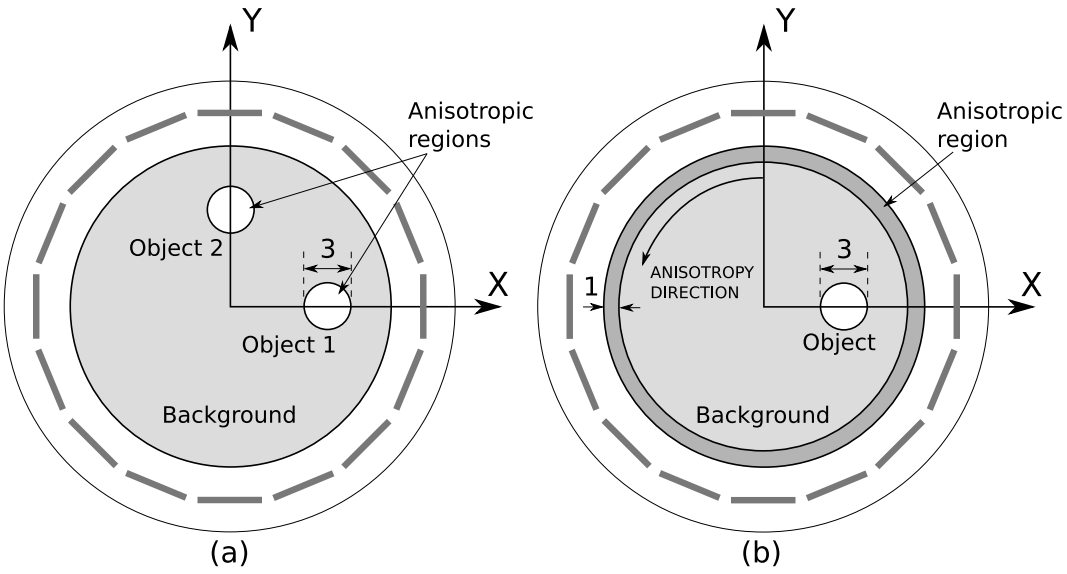


Figure 5.9: The cylindrical phantoms with different anisotropic electrical properties used in simulations.

Table 5.1: The conductivity values in S $m^{-1}$ of the simulation model shown in figure 5.9.

| | $\sigma_{xx}$ | $\sigma_{xy}$ | $\sigma_{xz}$ | $\sigma_{yy}$ | $\sigma_{yz}$ | $\sigma_{zz}$ |
|---|---|---|---|---|---|---|
| Object 1 | 1 | 0 | 0 | 2 | 0 | 1 |
| Object 2 | 2 | 0 | 0 | 1 | 0 | 1 |
| Background | 1 | 0 | 0 | 1 | 0 | 1 |

model is shown in figure 5.9-(a) and the corresponding conductivity values were given in table 5.1. The aim was to investigate the limitations of solvers that use an isotropic sensitivity matrix when the imaging target shows anisotropic properties and further investigate the possibility of anisotropic conductivity tensor imaging.

The second phantom was designed to see the effect of anisotropic muscle tissues that cover the rib cage in chest tomographies. To do so, an anisotropic layer of 1 cm thickness was assumed in the outermost shell of the phantom in order to reflect the muscle anisotropy (see, figure 5.9-(b)). As the target object for the reconstruction, a spherical, isotropic inhomogenetity of 3 cm diameter located at [5, 0, 0] cm was chosen. Knowing that the main axis of the anisotropic conductivity tensor resides on the transverse plane, the conductivity tensor associated with the voxels lying in the anisotropic layer was assigned

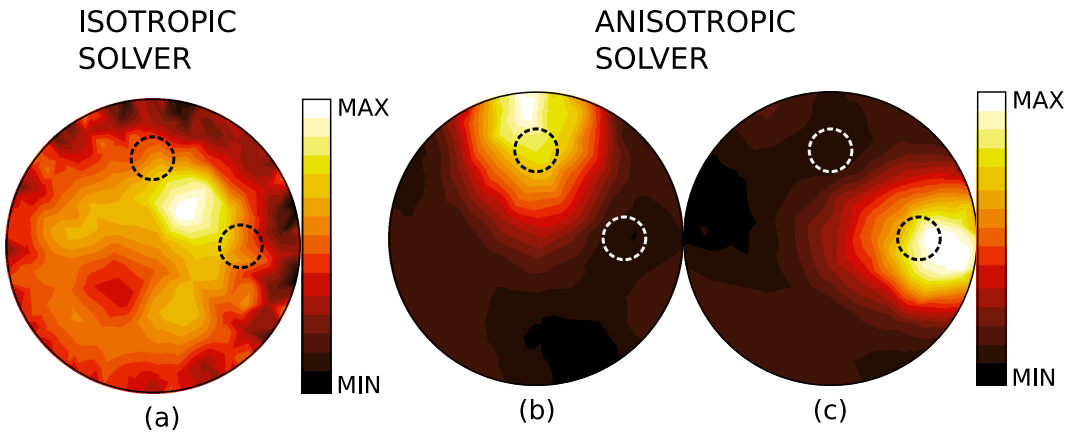


Figure 5.10: (a) Conductivity reconstruction of the central slice using an isotropic solver. Reconstruction of different conductivity tensor components: (b) $\Delta\sigma_{xx}$ reconstruction, (c) $\Delta\sigma_{yy}$ reconstruction.

by defining the tensor eigenvalues and the corresponding rotation matrix as follows,

$$\sigma(\alpha) = \mathbf{R}_\alpha e \mathbf{R}_\alpha^T, \tag{5.3}$$

where $e$ is the diagonal eigenvalue matrix, $\alpha$ is the polar angle of the voxel on the transverse plane and $\mathbf{R}_\alpha$ is the rotation matrix as defined below,

$$\mathbf{R}_\alpha = \begin{pmatrix} cos(\alpha) & -sin(\alpha) & 0 \\ sin(\alpha) & cos(\alpha) & 0 \\ 0 & 0 & 1 \end{pmatrix}. \tag{5.4}$$

$e$ was chosen as with the diagonal entries [1, 1.2, 1] S m$^{-1}$ assuming that the conductivity ratio of the longitudinal direction to the transverse direction along the muscle fibers is 1.2:1 at 500 kHz operating frequency [Rigaud et al., 1996].

### 5.3.3 Results

There are essentially two different elements of anisotropy in $\Delta\sigma = \mathbf{S}^\dagger \Delta v$: (1) The sensitivity matrix $\mathbf{S}$ and (2) the reference dataset $v_{ref}$ when calculating $\Delta v = v_p - v_{ref}$, $v_p$ denoting the perturbed voltage signal due to an anisotropic body. Both can be calculated from either an isotropic (iso) or anisotropic (aniso) model, so that we get four different combinations:

i. $\Delta\sigma_{iso,iso} = \mathbf{S}^{\dagger}_{iso}\Delta v_{iso}$

ii. $\Delta\sigma_{iso,aniso} = \mathbf{S}^{\dagger}_{iso}\Delta v_{aniso}$

iii. $\Delta\sigma_{aniso,iso} = \mathbf{S}^{\dagger}_{aniso}\Delta v_{iso}$

iv. $\Delta\sigma_{aniso,aniso} = \mathbf{S}^{\dagger}_{aniso}\Delta v_{aniso}$

where (i) is the well-known isotropic implementation and (iii) assumes an incorrect isotropic reference dataset for reconstruction. Similarly, (ii) and (iv) correspond to real measurement conditions (i.e., difference imaging) if anisotropy is involved. The reconstructions (ii) and (iv) were firstly analyzed by constructing a model as illustrated in figure 5.9-(a). A uniform background conductivity is assumed for the computation of the reference dataset and difference data is used for imaging. The corresponding images were reconstructed accordingly using both the isotropic and anisotropic sensitivity matrices. The isotropic sensitivity matrix is capable of reconstructing only a scalar distribution. However, the anisotropic sensitivity matrix leads to the reconstruction of the tensor components. As can be clearly recognized in figure 5.10, the isotropic reconstruction yields poor results and the quality of the images is not sufficient for the diagnosis of anomalies. The peak value of the image is unrelated to the anomaly locations and spurious artifacts were noted on the boundary. However, the anisotropic reconstruction of $\Delta\sigma_{xx}$ and $\Delta\sigma_{yy}$ yield better images and the anomalies can now be clearly distinguished. It was observed that the peak values of the images are slightly shifted from the center of the abnomalies to the boundary and the reconstructions are blurred.

Various conductivity reconstructions of the central slice of the second phantom are shown in figure 5.11. The images are obtained by applying different reference datasets and sensitivity maps, i.e. using anisotropic and isotropic models with different initializations. The images in the first row were reconstructed using an isotropic sensitivity map, and therefore the estimation is just one value per voxel. However, the images of the last three rows were reconstructed using an anisotropic sensitivity map. Only the reconstructed diagonal components of the conductivity tensor are presented, since the other

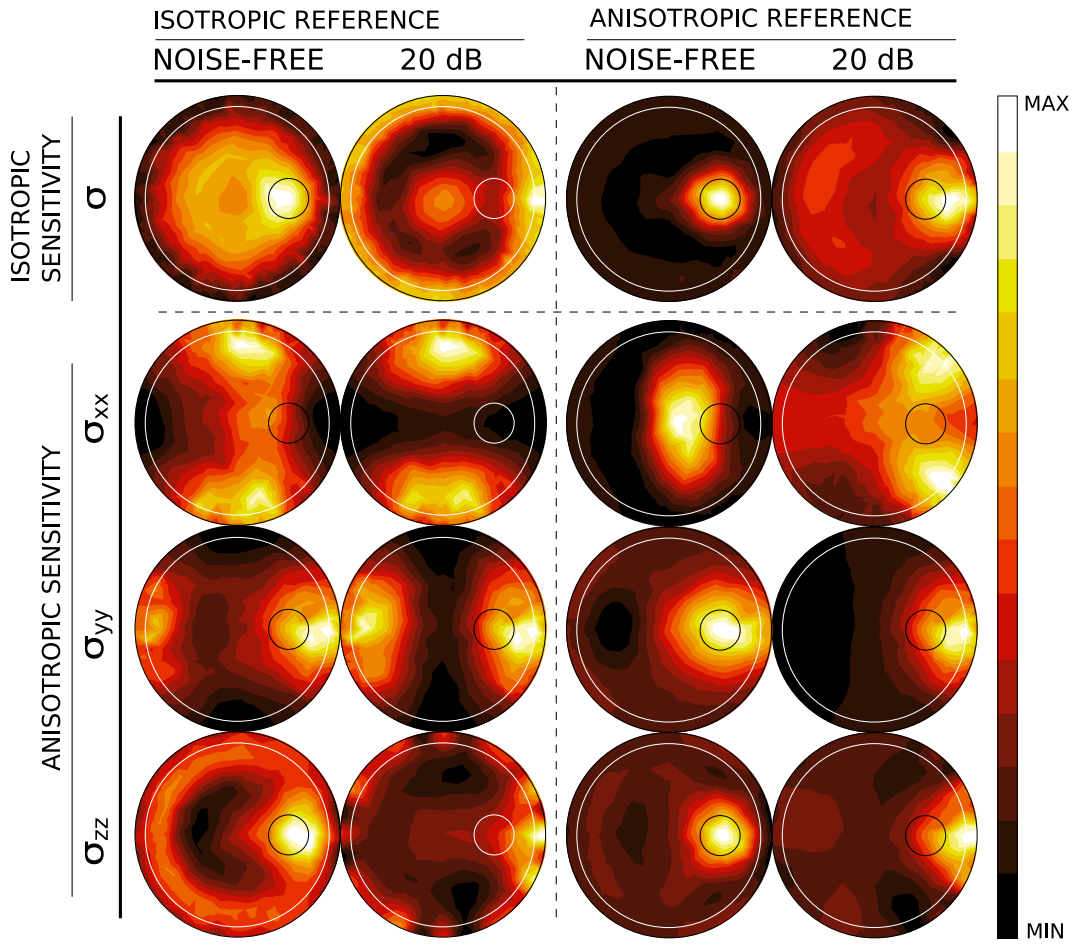


Figure 5.11: Various conductivity distribution reconstructions of the central slice obtained by applying different initializations and sensitivity maps.

components are negligibly small due to the nonexistent anisotropic components of the conductivity perturbation. The columns are divided into 2 groups of 2 columns each. Each group corresponds to the images where the reference data were simulated using the same model properties as for calculating the associated sensitivity matrix. In other words, the reference data of the left group were obtained using an isotropic model of uniform conductivity distribution, whereas the right group corresponds to the reference data that were simulated from an anisotropic model. The left column of each group presents the noise-free reconstructions and the right column shows the images obtained by adding a Gaussian noise of 20 dB SNR level (the noise is defined as in 3.10) to the difference voltage data. The colorbars of the images are scaled from the minimum to the maximum value independently.

The perturbation is hardly recognizable and spurious artifacts appeared, particularly lying on the boundary of the images, by using the isotropic sensitivity map and the isotropic reference data. However, better accuracy is achieved using the anisotropic dataset together with the isotropic sensitivity map. By looking at the corresponding tensor estimates, the isotropic reference data still gives poor results. The noise-free $\sigma_{xx}$ images are very blurred and suffer from poor localization. This is due to the low sensitivity of the system to the region where the inhomogeneity is present. The $\sigma_{yy}$ reconstructions are better localized compared to $\sigma_{xx}$ in that region; however, they still show diffuse characteristics. $\sigma_{zz}$ reconstructions were the best among others. Under noise, the reconstructed perturbation location is biased towards the positions where the sensitivity is better, i.e., it is moved usually towards the border, however, for $\sigma_{xx}$ the perturbation is split into 2 pieces and moved towards the borders.

### 5.3.4 Discussions

By simulations, the potential of anisotropic tensor imaging was demonstrated using the reconstruction of anomalies that have anisotropic characteristics. The conventional isotropic image reconstruction algorithms are found to be insufficient when the target is anisotrpoic. Additionally, the importance of

having or simulating an accurate reference dataset was adressed in order to reconstruct feasible and reliable images. In state differential or frequency differential variants of MIT this is naturally accomplished without any further consideration, however, the absolute imaging methods and user initialized inversion algorithms are found to yield very poor images even in the existence of a mild anisotropy. The selection of the sensitivity map, whether isotropic or anisotropic, did not notably influence the results unless the imaging targets show anisotropic characteristics. Interestingly, the isotropic reconstructions sometimes showed even better quality in images. This may be due to the strong effect of the longitidunal tensor component which is also the most accurate one.

Although different types of chest muscles that cover the ribs show up anisotropy in various directions, the simulations were conducted assuming a transversal anisotropy only. This simplification may not adequately reflect the true characteristics of the human body, nevertheless it is a better approximation of reality than using the previously used isotropic models. The future work may include building more realistic models based on the anatomy of the chest gathered from diffusion MRI-images.

## 5.4 Conclusion

The ultimate goal of MIT is to make the modality to be used for diagnostic and monitoring purposes in clinics, hospitals and emergency units. Although, several prototype experimental systems have been built [Korjenevsky et al., 2000, Scharfetter et al., 2008, Vauhkonen et al., 2008, Watson et al., 2008], there has been no system available for clinical use as yet. This is presumably due to the issues arising from inaccurate modeling which yield poor in vivo characteristics. Recent studies have proposed several modeling improvements such as building MRI-guided models that results in more realistic geometries [Zolgharni et al., 2009a,b]. Similarly, a part of this dissertation serves for that purpose and points out the importance of correcting the model by obtaining the patient positioning during data acquisition and investigates the effects

and consequences of anisotropic tissues in imaging and concludes that the anisotropic modeling works better for the reconstruction of anisotropic targets. Future work may include developing better movement tracking strategies and improving the imaging quality by applying proper regularization techniques for the anisotropic inversion and consideration of anatomical constraints.

# CHAPTER 6

# FUTURE DIRECTIONS

The following items summarize the possible and mostly essential steps to be concluded to improve the performance of the system and point out the open issues.

1. *Physiologically realistic models*: The image reconstruction in MIT is heavily dependent on the residuals between the estimated and measured quantities. Therefore, numerical models that closely mimic the human physiology, in principle, help to reduce the artifacts due to modeling inconsistencies and lead to better reconstructions. To date, there exist several studies using realistical body geometries segmenting the tissue regions from high resolution images obtained with an MRI or CT. Besides the realistical geometrical information, it may be equally important to construct models based on the anisotropy information that can be acquired from the diffusion tensor images.

2. *Patient specific models*: The use of MIT in ambulances or during the first intervention phase for the diagnosis of cerebral hemorrhage was previously proposed and there is an ongoing research on this. However, the patient information is usually very limited in these cases. Therefore, it is still not certain whether readily available and approximate sensitivity maps works successfully or not, because of the different characteristics of the patients such as size, age, sex and tissue properties. To investigate the robustness of the imaging performance for different patients, several

tissue and geometry statistics must be collected and a conclusion should be made based on the results.

3. *Optimal measurement frequencies*: All tissues have different electrical properties over the $\beta$-dispersion frequency region. Based on the applications, in order to increase contrast of the imaging target, optimal frequencies for several predefined applications such as head or chest must be determined. The research on hardware must be focused on the corresponding operating frequencies for different applications.

4. *Nonlinearity issues*: The relationship between the tissue electrical properties and measurements is highly nonlinear and the common approach is to assume linearity and solve for small perturbations. Therefore, choosing a good initialization for the inverse problem is not clearly investigated for realistic models. For this, it is important to investigate the degree of nonlinearity and explore the corresponding multi-modal inversion behavior in order to end up with better initializations and maintain the stability of inversion.

# Bibliography

M. Abramowitz and I. A. Stegun, editors. *Handbook of mathematical functions with formulas, graphs and mathematical tables.* Dover Publications, New York, ninth edition, 1970.

S. Al-Zeibak and N. H. Saunders. A feasibility study of in vivo electromagnetic imaging. *Physics in Medicine and Biology*, 38(1):151–160, 1993.

O. Bíro. Edge element formulations of eddy current problems. *Computer methods in applied mechanics and engineering*, 169(2-4):391–405, 1999.

M. Bollhöfer and Y. Saad. Multilevel preconditioners constructed from inverse-based ilus. *SIAM Journal on Scientific Computing*, 27(5):1627–1650, 2006.

K. G. Boone and D. S. Holder. Current approaches to analogue instrumentation design in electrical impedance tomography. *Physiological Measurement*, 17(4):229–247, 1996a.

K. G. Boone and D. S. Holder. Effect of skin impedance on image quality and variability in electrical impedance tomography: a model study. *Medical and Biological Engineering and Computing*, 34(5):351–354, 1996b.

P. Brunner, R. Merwa, A. Missner, J. Rosell, K. Hollaus, and H. Scharfetter. Reconstruction of the shape of conductivity spectra using differential multi-frequency magnetic induction tomography. *Physiological Measurement*, 27 (5):237–248, 2006.

T. M. Cover and J. A. Thomas. *Elements of information theory.* Wiley, New York, 2006.

A. Curtis. Optimal designs of focused experiments and surveys. *Geophysics Journal International*, 139(1):205–215, 1999.

N. G. Gençer and Y. Z. İder. A comparative study of several exciting magnetic fields for induced current eit. *Physiological Measurement*, 15(2A):A51–A57, 1994.

N. G. Gençer and M. N. Tek. Electrical conductivity imaging via contactless measurements. *Medical Imaging, IEEE Transactions on*, 18(7):617–627, 1999a.

N. G. Gençer and M. N. Tek. Forward problem solution for electrical conductivity imaging via contactless measurements. *Physics in Medicine and Biology*, 44(4):927–940, 1999b.

N. G. Gençer, M. Kuzuoğlu, and Y. Z. İder. Electrical impedance tomography using induced currents. *Medical Imaging, IEEE Transactions on*, 13(2): 338–350, 1994.

G. H. Golub and C. F. Van Loan, editors. *Matrix Computations*. Johns Hopkins Press, Baltimore, second edition, 1989.

H. Griffiths. Magnetic induction tomography. *Measurement Science and Technology*, 12(8):1126–1131, 2001.

H. Griffiths, W. R. Stewart, and W. Gough. Magnetic induction tomography: A measuring system for biological tissues. *Annals of the New York Academy of Sciences*, 873(1):335–345, 1999.

D. Gürsoy. Multi-frequency contactless electrical impedance imaging using realistic head models: Single coil simulations. Master's thesis, Middle East Technical University, 2007.

D. Gürsoy and H. Scharfetter. Reconstruction artefacts in magnetic induction tomography due to patient's movement during data acquisition. *Physiological Measurement*, 30(6):165–174, 2009a.

D. Gürsoy and H. Scharfetter. Optimum receiver array design for magnetic induction tomography. *Biomedical Engineering, IEEE Transactions on*, 56 (5):1435–1441, 2009b.

D. Gürsoy and H. Scharfetter. The effect of receiver coil orientations on the imaging performance of magnetic induction tomography. *Measurement Science and Technology*, 20(10):105505 (9pp), 2009c.

D. Gürsoy and H. Scharfetter. Anisotropic conductivity tensor imaging using magnetic induction tomography. *Physiological Measurement*, submitted.

P. C. Hansen. *Rank-deficient and discrete ill-posed problems*. SIAM, Philadelphia, 1998.

L. W. Hart, H. W. Ko, J. H. JR. Meyer, D. P. Vasholz, and R. I. Joseph. A noninvasive electromagnetic conductivity sensor for biomedical applications. *Biomedical Engineering, IEEE Transactions on*, 35(12):1011–1022, 1988.

J. C. Hellier. *Handbook of nondestructive evaluation*. McGraw-Hill, New York, 2001.

D. S. Holder, editor. *Clinical and physiological applications of electrical impedance tomography*. UCL Press, London, 1993.

D. S. Holder, editor. *Electrical impedance tomography: Methods, history and applications*. Institute of Physics Publishing, Bristol, 1995.

K. Hollaus, C. Magele, R. Merwa, and H. Scharfetter. Numerical simulation of the eddy current problem in magnetic induction tomography for biomedical applications by edge elements. *Magnetics, IEEE Transactions on*, 40(2): 623–626, 2004a.

K. Hollaus, C. Magele, R. Merwa, and H. Scharfetter. Fast calculation of the sensitivity matrix in magnetic induction tomography by tetrahedral edge finite elements and the reciprocity theorem. *Physiological Measurement*, 25 (1):159–168, 2004b.

C. H. Igney, S. Watson, R. J. Williams, H. Griffiths, and O. Dössel. Design and performance of a planar-array MIT system with normal sensor alignment. *Physiological Measurement*, 26(2):263–278, 2005.

D. D. Jackson. Interpretation of inaccurate, insufficient and inconsistent data. *Geophysical Journal of the Royal Astronomical Society*, 28:97–109, 1972.

H. P. Kao, E. Shwedyk, and E. R. Cardoso. Measurement of canine cerebral oedema using vector impedance methods. *Neurological Research*, 13(4):233–236, 1991.

B. Ü. Karbeyaz and N. G. Gençer. Electrical conductivity imaging via contactless measurements: An experimental study. *Medical Imaging, IEEE Transactions on*, 22(5):627–635, 2003.

A. A. Kaufman and Y. A. Dashevsky. *Principles of Induction Logging*. Elsevier Science Publishing, Amsterdam, first edition, 2003.

A. A. Kaufman and G. V. Keller. *Induction Logging*. Elsevier Science Publishing, New York, 1989.

A. V. Korjenevsky and V. A. Cherepenin. Magnetic induction tomography. *Journal of Communications Technology and Electronics*, 42:469–474, 1997.

A. V. Korjenevsky and V. A. Cherepenin. Progress in realization of magnetic induction tomography. *Annals of the New York Academy of Sciences*, 873 (1):346–352, 1999.

A. V. Korjenevsky, V. A. Cherepenin, and S. Sapetsky. Magnetic induction tomography: experimental realization. *Physiological Measurement*, 21(1): 89–94, 2000.

C. Ktistis, D. W. Armitage, and A. J. Peyton. Calculation of the forward problem for absolute image reconstruction in MIT. *Physiological Measurement*, 29(6):455–464, 2008.

X. Ma, A. J. Peyton, S. R. Higson, A. Lyons, and S. J. Dickinson. Hardware and software design for an electromagnetic induction tomography (EMT)

system for high contrast metal process applications. *Measurement Science and Technology*, 17(1):111–118, 2006.

X. Ma, A. J. Peyton, S. R. Higson, and P. Drake. Development of multiple frequency electromagnetic induction systems for steel flow visualization. *Measurement Science and Technology*, 19(9):094008 (9pp), 2008.

J. Malmivuo and R. Plonsey. *Bioelectromagnetism: principles and applications of bioelectric and biomagnetic fields*. Oxford University Press, New York, 1995.

E. T. McAdams and J. Jossinet. Tissue impedance: A historical overview. *Physiological Measurement*, 16(3A):A1–A13, 1995.

R. Merwa and H. Scharfetter. Magnetic induction tomography: Evaluation of the point spread function and analysis of resolution and image distortion. *Physiological Measurement*, 28(7):313–324, 2007.

R. Merwa and H. Scharfetter. Magnetic induction tomography: Comparison of the image quality using different types of receivers. *Physiological Measurement*, 29(6):417–429, 2008.

R. Merwa, K. Hollaus, B. Brandstatter, and H. Scharfetter. Numerical solution of the general 3D eddy current problem for magnetic induction tomography (spectroscopy). *Physiological Measurement*, 24(2):545–554, 2003.

R. Merwa, K. Hollaus, O. Biró, and H. Scharfetter. Detection of brain oedema using magnetic induction tomography: a feasibility study of the likely sensitivity and detectability. *Physiological Measurement*, 25(1):347–354, 2004.

R. Merwa, K. Hollaus, P. Brunner, and H. Scharfetter. Solution of the inverse problem of magnetic induction tomography (MIT). *Physiological Measurement*, 26(2):241–250, 2005.

R. Merwa, P. Brunner, A. Missner, K. Hollaus, and H. Scharfetter. Solution of the inverse problem of magnetic induction tomography (MIT) with multiple objects: analysis of detectability and statistical properties with respect to

the reconstructed conducting region. *Physiological Measurement*, 27(5):249–259, 2006.

A. Morris, H. Griffiths, and W. Gough. A numerical model for magnetic induction tomographic measurements in biological tissues. *Physiological Measurement*, 22(1):113–119, 2001.

J. R. Mortarelli. A generalization of the geselowitz relationship useful in impedance plethysmographic field calculations. *Biomedical Engineering, IEEE Transactions on*, BME-27(11):665–667, 1980.

J. Netz, E. Forner, and S. Haagemann. Contactless impedance measurement by magnetic induction - a possible method for investigation of brain impedance. *Physiological Measurement*, 14(4):463–471, 1993.

M. Osypka and E. Gersing. Tissue impedance spectra and the appropriate frequencies for eit. *Physiological Measurement*, 16(3A):A49–A55, 1995.

A. J. Peyton, Z. Z. Yu, G. Lyon, S. Al-Zeibak, J. Ferreira, J. Velez, F. Linhares, A. R. Borges, H. L. Xiong, N. H. Saunders, and M. S. Beck. An overview of electromagnetic inductance tomography: description of three different systems. *Measurement Science and Technology*, 7(3):261–271, 1996.

M. H. Pham and A. J. Peyton. A model for the forward problem in magnetic induction tomography using boundary integral equations. *Magnetics, IEEE Transactions on*, 44(10):2262–2267, 2008a.

M. H. Pham and A. J. Peyton. Computation of 3-D sensitivity coefficients in magnetic induction tomography using boundary integral equations and radial basis functions. *Magnetics, IEEE Transactions on*, 44(10):2268–2276, 2008b.

C. H. Riedel, M. Keppelen, S. Nani, R. D. Merges, and O. Dössel. Planar system for magnetic induction conductivity measurement using a sensor matrix. *Physiological Measurement*, 25(1):403–411, 2004.

B. Rigaud, J. P. Morucci, and N. Chauveau. Bioelectrical techniques in medicine: Part I: Bioimpedance measurement. second section: impedance spectrometry. *Critical Reviews in Biomedical Engineering*, 24(4-6):257–351, 1996.

J. Rosell, R. Casanas, and H. Scharfetter. Sensitivity maps and system requirements for magnetic induction tomography using a planar gradiometer. *Physiological Measurement*, 22(1):121–130, 2001.

J. Rosell, R. Merwa, P. Brunner, and H. Scharfetter. A multifrequency magnetic induction tomography system using planar gradiometers: Data collection and calibration. *Physiological Measurement*, 27(5):271–280, 2006.

H. Scharfetter, H. K. Lackner, and J. Rosell. Magnetic induction tomography: Hardware for multi-frequency measurements in biological tissues. *Physiological Measurement*, 22(1):131–146, 2001.

H. Scharfetter, P. Riu, M. Populo, and J. Rosell. Sensitivity maps for low-contrast perturbations within conducting background in magnetic induction tomography. *Physiological Measurement*, 23(1):195–202, 2002.

H. Scharfetter, R. Casanas, and J. Rosell. Biological tissue characterization by magnetic induction spectroscopy (MIS): Requirements and limitations. *Biomedical Engineering, IEEE Transactions on*, 50(7):870–880, 2003.

H. Scharfetter, S. Rauchenzauner, R. Merwa, O. Biró, and K. Hollaus. Planar gradiometer for magnetic induction tomography (MIT): Theoretical and experimental sensitivity maps for a low-contrast phantom. *Physiological Measurement*, 25(1):325–333, 2004.

H. Scharfetter, R. Merwa, and K. Pilz. A new type of gradiometer for the receiving circuit of magnetic induction tomography (MIT). *Physiological Measurement*, 26(2):307–318, 2005.

H. Scharfetter, K. Hollaus, J. Rosell, and R. Merwa. Single-step 3-D image reconstruction in magnetic induction tomography: Theoretical limits of spa-

tial resolution and contrast to noise ratio. *Annals of Biomedical Engineering*, 34(11):1786–1798, 2006.

H. Scharfetter, A. Köstinger, and S. Issa. Hardware for quasi-single-shot multifrequency magnetic induction tomography (MIT): The Graz Mk2 system. *Physiological Measurement*, 29(6):431–443, 2008.

W. R. Smythe. *Static and dynamic electricity*. McGraw Hill, New York, second edition, 1950.

M. Soleimani. Sensitivity maps in three-dimensional magnetic induction tomography. *Insight - Non-Destructive Testing and Condition Monitoring*, 48 (1):39–44, 2006.

M. Soleimani and W. R. B. Lionheart. Absolute conductivity reconstruction in magnetic induction tomography using a nonlinear method. *Medical Imaging, IEEE Transactions on*, 25(12):1521–1530, 2006.

M. Soleimani, W. R. B. Lionheart, A. J. Peyton, X. Ma, and S. R. Higson. A three-dimensional inverse finite-element method applied to experimental eddy-current imaging data. *Magnetics, IEEE Transactions on*, 42(5):1560–1567, 2006.

M. Soleimani, A. Adler, T. Dai, and A. J. Peyton. Application of a single step temporal imaging of magnetic induction tomography for metal flow visualisation. *Insight - Non-Destructive Testing and Condition Monitoring*, 50(1):25–29, 2008.

M. Vauhkonen, M. Hamsch, and C. H. Igney. A measurement system and image reconstruction in magnetic induction tomography. *Physiological Measurement*, 29(6):445–454, 2008.

J. R. Wait. *Geo-Electromagnetism*. Academic Press, New York, 1982.

S. Watson, A. Morris, R. J. Williams, H. Griffiths, and W. Gough. A primary field compensation scheme for planar array magnetic induction tomography. *Physiological Measurement*, 25(1):271–279, 2004.

S. Watson, C. H. Igney, R. J. Williams O. Dössel, and H. Griffiths. A comparison of sensors for minimizing the primary signal in planar-array magnetic induction tomography. *Physiological Measurement*, 26(2):319–331, 2005.

S. Watson, R. J. Williams, W. Gough, and H. Griffiths. A magnetic induction tomography system for samples with conductivities below 10 s $m^{-1}$. *Measurement Science and Technology*, 19(4):045501 (11pp), 2008.

Z. Xu, H. Luo, W. He, C. He, X. Song, and Z. Zahng. A multi-channel magnetic induction tomography measurement system for human brain model imaging. *Physiological Measurement*, 30(6):175–186, 2009.

J. Zhang and R. P. Patterson. EIT images of ventillation: what contributes to the resistivity changes? *Physiological Measurement*, 26(2):81–92, 2005.

M. Ziolkowski, S. Gratkowski, and R. Palka. Solution of three dimensional inverse problem of magnetic induction tomography using tikhonov regularization method. *International Journal of Applied Electromagnetics and Mechanics*, 30(3-4):245–253, 2009.

M. Zolgharni, P. D. Ledger, D. W. Armitage, D. S. Holder, and H. Griffiths. Imaging cerebral haemorrhage with magnetic induction tomography: Numerical modeling. *Physiological Measurement*, 30(6):187–200, 2009a.

M. Zolgharni, P. D. Ledger, and H. Griffiths. Forward modelling of magnetic induction tomography: a sensitivity study for detecting haemorrhagic cerebral stroke. *Medical and Biological Engineering and Computing*, 2009b.

# APPENDIX A

# MAGNETIC VECTOR POTENTIAL

hTe azimuthal component of the magnetic vector potential in cylindrical coordinates $(\rho, \phi, z)$ of a circular coil with radius $a$ and carrying a current $I$ can be calculated from [Smythe, 1950],

$$A_\phi = \frac{\mu I}{\pi k}\left(\frac{a}{\rho}\right)^{1/2}\left(\left(1-\frac{1}{2}k^2\right)K - E\right), \tag{A.1}$$

where $k^2$ is defined as,

$$k^2 = 4a\rho\left((a+\rho)^2 + z^2\right)^{-1}, \tag{A.2}$$

and $K$ and $E$ are the complete elliptic integrals of the first and second kind, as given below,

$$K(m) = \int_0^1 \left(\frac{t^2}{(1-t)(1-m^2t^2)}\right)^{1/2} dt, \tag{A.3}$$

$$E(m) = \int_0^1 \left(\frac{1-m^2t^2}{1-t^2}\right)^{1/2} dt, \tag{A.4}$$

where $0 \leq m \leq 1$ and $m = k^2$. $K$ and $E$ can be computed either by a numerical quadrature or by using a polynomial approximation as described in [Abramowitz and Stegun, 1970].

# APPENDIX B

# OPTIMIZATION MEASURE

In information theory, the mutual information of two random variables is a quantity that measures the mutual dependence of the two variables and will provide a basis for the optimization. Let $\mathbf{d} = [d_1, d_2]$ be the data vector consisting of two channels and have a multivariate normal distribution with mean vector $\mu_d$ and covariance matrix $\mathbf{C}_d$. If the covariance matrix of the model parameters is assumed to be an identity matrix then,

$$\mathbf{C}_d = \mathbf{S}\mathbf{S}^T = \begin{bmatrix} (\mathbf{s}_1 \cdot \mathbf{s}_1) & (\mathbf{s}_1 \cdot \mathbf{s}_2) \\ (\mathbf{s}_1 \cdot \mathbf{s}_2) & (\mathbf{s}_2 \cdot \mathbf{s}_2) \end{bmatrix}. \tag{B.1}$$

The mutual information between these two data [Cover and Thomas, 2006] is,

$$\begin{aligned} I(d_1; d_2) &= H(d_1) + H(d_2) - H(d_1, d_2) && \text{(B.2)} \\ &= -\frac{1}{2} log \left( 1 - \frac{(\mathbf{s}_1 \cdot \mathbf{s}_2)^2}{(\mathbf{s}_1 \cdot \mathbf{s}_1)(\mathbf{s}_2 \cdot \mathbf{s}_2)} \right). && \text{(B.3)} \end{aligned}$$

By noting that $(\mathbf{s}_1 \cdot \mathbf{s}_2)^2/(\mathbf{s}_1 \cdot \mathbf{s}_1)(\mathbf{s}_2 \cdot \mathbf{s}_2) \in [0, 1]$, minimizing the mutual information between two data can be equivalently established by maximizing the following function,

$$q_{12} = 1 - \left( \frac{\mathbf{s}_1 \cdot \mathbf{s}_2}{\|\mathbf{s}_1\| \, \|\mathbf{s}_2\|} \right)^2, \tag{B.4}$$

where $q$ can be defined as a quality measure between the two data. Let there be $N$ independent data and $K$ different transmitters influencing a single receiver, then, the average quality for that receiver is written as,

$$Q_r = \frac{1}{KN} \sum_{k=1}^{K} \sum_{n=1}^{N} \left( \frac{q_{kn} + q_{nk}}{2} \right). \tag{B.5}$$

# VITA

Doğa Gürsoy was born in Ankara, Turkey, in October 1981. He received the BSc and MSc degrees in electrical and electronics engineering from the Middle East Technical University (METU), Ankara, Turkey, in 2004 and 2007, respectively, and PhD degree in electrical engineering, from the Graz University of Technology, Graz, Austria, in 2010.

From 2006 to 2007, he was a Research Assistant at the Department of Electrical and Electronics Engineering, METU. Since 2007, he has been working as a Research Assistant at the Institute of Medical Engineering, Graz University of Technology. During his PhD, he was involved as a researcher in the project "Mathematical Optimization and Application in Biomedical Sciences: Near-Field Techniques for Biomedical Imaging" granted by the Austrian Science Fund. He has published in peer reviewed international journals and contributed at conferences. He served as a referee for several Journals including Inverse Problems, Physics in Medisince and Biology, Philosophical Transactions and International Journal of Infrared and Millimeter Waves. He was one of the founders of the SIAM Student Chapter of Graz and he served as President of the Chapter in 2009. He is a member of IEEE, SIAM and ÖGBMT. His current interests include medical imaging, electromagnetic modeling, and inverse problems.

# PUBLICATIONS

**International Journal Papers (Peer Reviewed):**

1. D. Gürsoy and H. Scharfetter. Anisotropic conductivity tensor imaging using magnetic induction tomography. *Physiological Measurement*, (under revision).

2. D. Gürsoy and H. Scharfetter. The effect of receiver coil orientations on the imaging performance of magnetic induction tomography. *Measurement Science and Technology*, 20(10):105505 (9pp), 2009.

3. D. Gürsoy and H. Scharfetter. Optimum receiver array design for magnetic induction tomography. *Biomedical Engineering, IEEE Transactions on*, 56(5):1435–1441, 2009.

4. D. Gürsoy and H. Scharfetter. Reconstruction artefacts in magnetic induction tomography due to patient's movement during data acquisition. *Physiological Measurement*, 30(6):165–174, 2009.

**Patent:**

1. H. Scharfetter and D. Gürsoy. Device and method for tracking the movements of the object to be measured in magnetic induction tomography. *European Patent Office*, (under revision).

**Conference Contributions:**

1. H. Scharfetter, S. Issa and D. Gürsoy. Tracking of object movements for artefact suppression in magnetic induction tomography (MIT) *International Conference on Electrical Bioimpedance*, Gainesville FL, USA, 2010.

2. D. Gürsoy and H. Scharfetter. A non-contact method for imaging the posterior chest using magnetic induction principles to monitor pulmonary oedema. *International Conference on Electrical Bioimpedance*, Gainesville FL, USA, 2010.

3. D. Gürsoy and H. Scharfetter. Feasibility of lung imaging using magnetic induction tomography. *Medical Physics and Biomedical Engineering World Congress*, Munich, Germany, 2009.

4. H. Scharfetter and D. Gürsoy. The effect of receiver coil orientations on the performance of magnetic induction tomography, *Medical Physics and Biomedical Engineering World Congress*, Munich, Germany, 2009.

5. D. Gürsoy and H. Scharfetter. The effect of anisotropic tissues on the reconstructed images of magnetic induction tomography. *10th International Conference on Biomedical Application of Electrical Impedance Tomography*, Manchester, United Kingdom, 2009.

6. H. Scharfetter, S. Issa and D. Gürsoy. Image reconstruction in magnetic induction tomography without using a phase reference channel, *10th International Conference on Biomedical Application of Electrical Impedance Tomography*, Manchester, United Kingdom, 2009.

7. D. Gürsoy. A sensor optimization algorithm to increase the stability of the magnetic induction tomography inversion. *Conference on Applied Inverse Problems*, Vienna, Austria, 2009.

8. D. Gürsoy and H. Scharfetter. Resolution and stability analysis of 16 channel magnetic induction tomography. *14th National Biomedical Engineering Meeting*, İzmir, Turkey, 2009.

9. D. Gürsoy and H. Scharfetter. Feasibility of head imaging using multifrequency magnetic induction tomography. *14th National Biomedical Engineering Meeting*, İzmir, Turkey, 2009.

10. D. Gürsoy and H. Scharfetter. Reconstruction artefacts in magnetic induction tomography due to patient's movement during data acquisition. *9th International Conference on Biomedical Applications of Electrical Impedance Tomography*, Hanover NH, USA, 2008.